

## Article

# Selective Adsorption Behavior and Mechanism for Cd(II) in Aqueous Solution with a Recoverable Magnetic-Surface Ion-Imprinted Polymer

Siqing Ye <sup>1</sup>, Weiye Zhang <sup>1</sup> , Xingliang Hu <sup>2</sup>, Hongxing He <sup>1,\*</sup> , Yi Zhang <sup>1</sup>, Weili Li <sup>3</sup>, Guangyuan Hu <sup>3</sup>, Yue Li <sup>3</sup> and Xiujun Deng <sup>3,\*</sup>

- <sup>1</sup> Yunnan Key Laboratory of Food Safety Testing Technology, College of Chemistry and Chemical Engineering, Kunming University, Kunming 650214, China; 18860965309@163.com (S.Y.); zhangviye@icloud.com (W.Z.)  
<sup>2</sup> Kunming Lüdao Environmental Technology Co., Ltd., Kunming 650228, China  
<sup>3</sup> Yunnan Key Laboratory of Metal-Organic Molecular Materials and Device, School of Chemistry and Chemical Engineering, Kunming University, Kunming 650214, China  
\* Correspondence: hxhe0212@kmu.edu.cn (H.H.); kmxydxj@126.com (X.D.)

**Abstract:** A novel recoverable magnetic Cd(II) ion-imprinted polymer was synthesized on the surface of silica-coated Fe<sub>3</sub>O<sub>4</sub> particles via the surface imprinting technique and chemical grafting method. The resulting polymer was used as a highly efficient adsorbent for the removal of Cd(II) ions from aqueous solutions. The adsorption experiments revealed that Fe<sub>3</sub>O<sub>4</sub>@SiO<sub>2</sub>@IIP had a maximum adsorption capacity of up to 29.82 mg·g<sup>-1</sup> for Cd(II) at an optimal pH of 6, with the adsorption equilibrium achieved within 20 min. The adsorption process followed the pseudo-second-order kinetic model and the Langmuir isotherm adsorption model. Thermodynamic studies showed that the adsorption of Cd(II) on the imprinted polymer was spontaneous and entropy-increasing. Furthermore, the Fe<sub>3</sub>O<sub>4</sub>@SiO<sub>2</sub>@IIP could rapidly achieve solid–liquid separation in the presence of an external magnetic field. More importantly, despite the poor affinity of the functional groups constructed on the polymer surface for Cd(II), we improved the specific selectivity of the imprinted adsorbent for Cd(II) through surface imprinting technology. The selective adsorption mechanism was verified by XPS and DFT theoretical calculations.

**Keywords:** ion-imprinted polymer; magnetic separation; Cd(II) ion; selective adsorption; density functional theory



**Citation:** Ye, S.; Zhang, W.; Hu, X.; He, H.; Zhang, Y.; Li, W.; Hu, G.; Li, Y.; Deng, X. Selective Adsorption Behavior and Mechanism for Cd(II) in Aqueous Solution with a Recoverable Magnetic-Surface Ion-Imprinted Polymer. *Polymers* **2023**, *15*, 2416. <https://doi.org/10.3390/polym15112416>

Academic Editor: Daniela Suteu

Received: 14 April 2023

Revised: 18 May 2023

Accepted: 19 May 2023

Published: 23 May 2023



**Copyright:** © 2023 by the authors. Licensee MDPI, Basel, Switzerland. This article is an open access article distributed under the terms and conditions of the Creative Commons Attribution (CC BY) license (<https://creativecommons.org/licenses/by/4.0/>).

## 1. Introduction

Cadmium is considered a highly toxic metal with high bioaccumulation potential and migratory capacity in water, and its presence can adversely affect human health (as a carcinogen and teratogen causing damage to the kidneys and brain) and aquatic ecosystems (by inhibiting physiological processes) [1]. Anthropogenic activities, such as metallurgical industries, mining operations, agricultural sectors, and paint industries, are the primary sources of increased cadmium concentrations in water [2]. The World Health Organization and the Ministry of Ecology and Environment of the PRC have established upper limits for Cd(II) concentrations in drinking water at 0.003 mg·L<sup>-1</sup> and 0.005 mg·L<sup>-1</sup>, respectively, to prevent adverse effects on human health and aquatic ecosystems [3,4]. Consequently, the removal of Cd(II) from aqueous solutions is of great significance, and efficient techniques for this purpose are highly sought after. Adsorption is a cost-effective and efficient method for removing Cd(II) from environmental water systems, but traditional adsorbents lack the ability to selectively separate target metal ions, thus limiting their application [5].

Ion-imprinted polymers (IIPs) are highly desirable due to their selectivity for target ions in the presence of competing ions. They are a type of biomimetic polymer material prepared using imprinted ions as templates and possessing a specific memory and the

ability to recognize imprinted ions [6,7]. IIPs have several advantages, including specific recognition, predictable conformation, and easy operation. However, traditional IIPs suffer from the imprinted sites embedded within the polymer network having poor accessibility, which results in low mass transfer rates for target ions [8,9]. Surface ion-imprinting technology (SIIT) has been developed to combat these limitations [10]. The technique consists of grafting imprinting sites onto the matrix's surface, improving the speed and ease of the target metal ion's binding to the imprinting sites. Surface ion-imprinted polymers (SIIPs) synthesized with SIIT exhibit advantageous properties, such as high selectivity, more accessible sites, high adsorption capacity, and fast mass transfer rates [11]. Montmorillonite [12], mesoporous silica [13], multi-walled carbon nanotubes [14], and  $\text{Fe}_3\text{O}_4$  nanoparticles [15] have been widely used as matrix materials.  $\text{Fe}_3\text{O}_4$  nanoparticles possess superparamagnetism and a high specific surface area and their surfaces can be easily modified, enabling rapid separation under the action of an external magnetic field. They effectively solve the solid–liquid separation problems affecting imprinted materials in solution, enhance the efficiency of separation and recovery, and hold promising development prospects [16].

2-Phosphonobutane-1,2,4-tricarboxylic acid (PBTCA) is an environmentally friendly, phosphonic acid-based surfactant that contains both carboxyl and phosphonic groups in a single molecule. PBTCA has been shown to improve the coordination of heavy metal ions [17]. Huang et al. developed a novel adsorbent by modifying chitosan-coated magnetic silica nanoparticles with PBTCA and demonstrated its ability to selectively adsorb uranium from aqueous solutions [18]. Cao et al. reported that adding PBTCA to plant agents significantly improved the capabilities for removal of heavy metals, such as Cd(II), Pb(II), and Zn(II), from contaminated soil [19]. To date, however, there is no research documenting the use of surface-imprinted magnetic polymers that employ PBTCA as an imprint site to selectively remove Cd(II) from aqueous solutions.

In this study, a novel magnetic imprinted polymer was developed utilizing SIIT with Cd(II) as the template molecule,  $\text{Fe}_3\text{O}_4$  as the magnetic core, and PBTCA as the functional monomer. Chemical grafting and imprinting techniques were employed to introduce carboxyl and phosphonic acid functional groups onto the surface of  $\text{Fe}_3\text{O}_4$  nanoparticles, resulting in a selective adsorbent for Cd(II) removal from aqueous solutions. Batch adsorption experiments were conducted to evaluate the adsorption performance of the imprinted adsorbent for Cd(II). The samples were characterized with several techniques, including FTIR, TEM, EDS, VSM, and TGA. Furthermore, XPS and DFT calculations were utilized to analyze the selective adsorption mechanism of the adsorbent for Cd(II).

## 2. Materials and Methods

### 2.1. Reagents

HCl and NaOH were purchased from Kolon Chemical Co., Ltd. (Chengdu, China).  $\text{Ni}(\text{NO}_3)_2 \cdot 6\text{H}_2\text{O}$ ,  $\text{Co}(\text{NO}_3)_2 \cdot 7\text{H}_2\text{O}$ ,  $\text{Zn}(\text{NO}_3)_2 \cdot 7\text{H}_2\text{O}$ , and  $\text{Cd}(\text{NO}_3)_2 \cdot 4\text{H}_2\text{O}$  were purchased from Beijing Chemical Plant (Beijing, China). Ammonium persulfate and sodium bisulfate were purchased from Windship Chemical Reagent Technology Co. (Tianjin, China). *N,N'*-Methylenebisacrylamide (MBA) was purchased from Maclean Biochemical Technology Co. (Shanghai, China). 2-Phosphonobutane-1,2,4-tricarboxylic acid (PBTCA) was purchased from Aladdin Biochemical Technology Co. (Shanghai, China). All aqueous solutions were prepared with deionized water.

### 2.2. Synthesis of $\text{Fe}_3\text{O}_4@SiO_2@IIP$

The core-shell magnetic  $\text{Fe}_3\text{O}_4@SiO_2@IIP$  nanospheres were obtained using surface ion-imprinting technology and the chemical grafting method, and the synthesis procedure is shown in Figure 1.

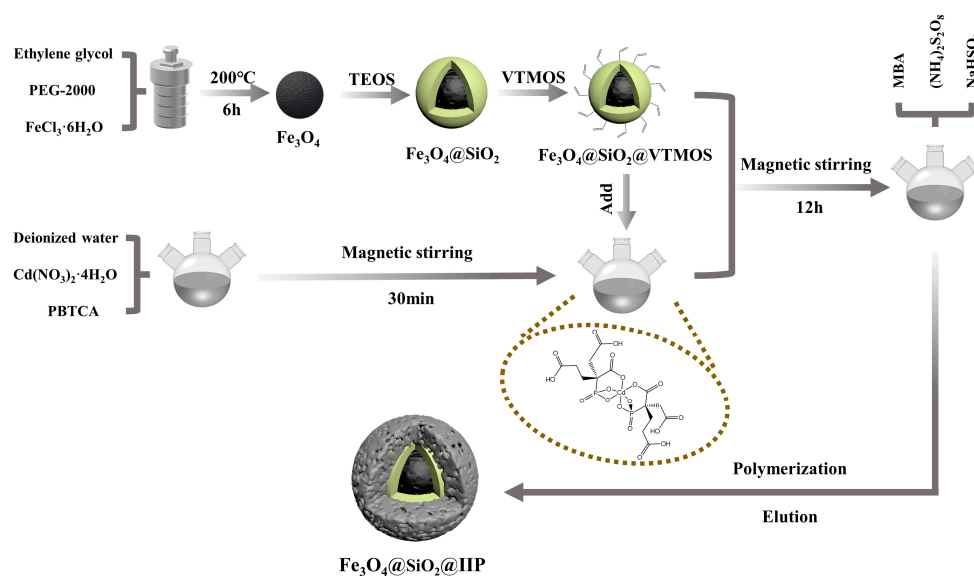


**Figure 1.** Schematic illustration of preparation of Cd(II)-IIP.

First, the vinyl-modified magnetic matrix material  $\text{Fe}_3\text{O}_4@\text{SiO}_2@\text{VTMOS}$  was prepared according to our previous report [20]. Second, the  $\text{Fe}_3\text{O}_4@\text{SiO}_2@\text{IIP}$  nanospheres were prepared with the following steps. Briefly, 3 mmol  $\text{Cd}(\text{NO}_3)_2 \cdot 4\text{H}_2\text{O}$  and 1 mmol PBTCa were added to 50 mL deionized water and stirred magnetically at room temperature. After stirring for 0.5 h, 0.15 g  $\text{Fe}_3\text{O}_4@\text{SiO}_2@\text{VTMOS}$  was added and stirred for 12 h. Then, 8 mmol MBA, 0.1 g ammonium persulfate, and 0.1 g sodium bisulfite were added, bubbled with high-purity argon for 30 min to eliminate oxygen, and sealed. After that, the mixture was heated in a water bath at 50 °C and magnetically stirred for 5 h. Finally, the obtained polymers were separated with a magnet; washed with methanol, hydrochloric acid, and deionized water to neutrality; and dried in a vacuum at 40 °C for 12 h to obtain  $\text{Fe}_3\text{O}_4@\text{SiO}_2@\text{IIP}$ .

The synthesis of the  $\text{Fe}_3\text{O}_4@\text{SiO}_2@\text{NIP}$  adsorbent was roughly the same as the above steps, except that  $\text{Cd}(\text{NO}_3)_2 \cdot 4\text{H}_2\text{O}$  was not introduced and HCl was not used for washing.

### 2.3. Adsorption Experiments

Batch adsorption experiments were performed by adding a certain amount of sorbent to a certain volume of metal ion solution. The mixture was shaken for a certain time at 25 °C. The concentrations of all metal ions were determined with ICP-AES. Each adsorption experiment was conducted in triplicate. The adsorption capacity was calculated according to Equation (1) [21]:

$$q = \frac{c_i - c_f}{1000W} \times V \quad (1)$$

where  $q$  ( $\text{mg} \cdot \text{g}^{-1}$ ) is the adsorption capacity;  $c_i$  ( $\text{mg} \cdot \text{L}^{-1}$ ) and  $c_f$  ( $\text{mg} \cdot \text{L}^{-1}$ ) are the initial and final concentrations of metal ions, respectively;  $V$  (mL) is the volume of the solution; and  $W$  (g) is the amount of sorbent.

### 2.4. Selectivity Study

In the selective adsorption experiment, 10 mg of the adsorbents  $\text{Fe}_3\text{O}_4@\text{SiO}_2@\text{IIP}$  or NIP was added to 20 mL of a  $5 \text{ mg} \cdot \text{L}^{-1}$  mixture of Cd(II), Ni(II), Co(II), and Zn(II) at solution pH = 6 and shaken for 1 h. Finally, the ion concentration in the filtrate was detected with ICP-AES. The distribution ratio ( $D$ ), the selectivity coefficient ( $k$ ) and the relative selectivity coefficient ( $k'$ ) were calculated according to Equations (2)–(4) [22]:

$$D = \frac{(c_0 - c_e)}{c_e} \times \frac{V}{W} \quad (2)$$

$$k = \frac{D_{Cd}}{D_M} \quad (3)$$

$$k' = \frac{k_{IIP}}{k_{NIP}} \quad (4)$$

where  $c_0$  ( $\text{mg}\cdot\text{L}^{-1}$ ) and  $c_e$  ( $\text{mg}\cdot\text{L}^{-1}$ ) are the initial and equilibrium concentrations of metal ions and  $M$  represents other competitive metal ions.

### 2.5. DFT Calculations

DFT calculations were performed using Gaussian 16W to obtain the adsorption energy. The system was optimized in aqueous solution using a PBE1PBE/def2svp basis set and D3(BJ) dispersion energy correction. After convergence, the def2tzvp basis set was used to calculate the adsorption energy ( $E_{ad}$ ). The adsorption energy ( $E_{ad}$ ) between the PTBCA molecule and different metal ions was calculated using Equation (5) [23]:

$$E_{ad} = E_{(total)} - E_{(PBTCa)} - E_{(adsorbates)} \quad (5)$$

where  $E_{(total)}$ ,  $E_{(PBTCa)}$ ,  $E_{(adsorbates)}$  are the total energy of the adsorption complex, the PTBCA molecule and the adsorbates, respectively.

## 3. Results

### 3.1. Characterization

#### 3.1.1. TEM

Figure 2 shows the TEM images of  $\text{Fe}_3\text{O}_4@\text{SiO}_2$  and  $\text{Fe}_3\text{O}_4@\text{SiO}_2@\text{IIP}$ . The sequentially coated  $\text{SiO}_2$  and PBTCa imprinted layers still maintained the spherical structure with good dispersion and did not appear to be clustered. In addition, the nucleus in the dark part represents  $\text{Fe}_3\text{O}_4$  nanoparticles, the inner layer with medium contrast is the silica shell, and the outer layer with light contrast is the PBTCa imprinted layer [22]. Figure 2(a) confirms the successful modification of  $\text{Fe}_3\text{O}_4$  nanoparticles through the silica layer with a particle size of about 519.1 nm, and Figure 2(b) shows a significant increase in the thickness of the magnetic-carrier cladding layer with a particle size of about 783.7 nm. In summary, the results showed that  $\text{Fe}_3\text{O}_4@\text{SiO}_2@\text{IIP}$  was prepared successfully.

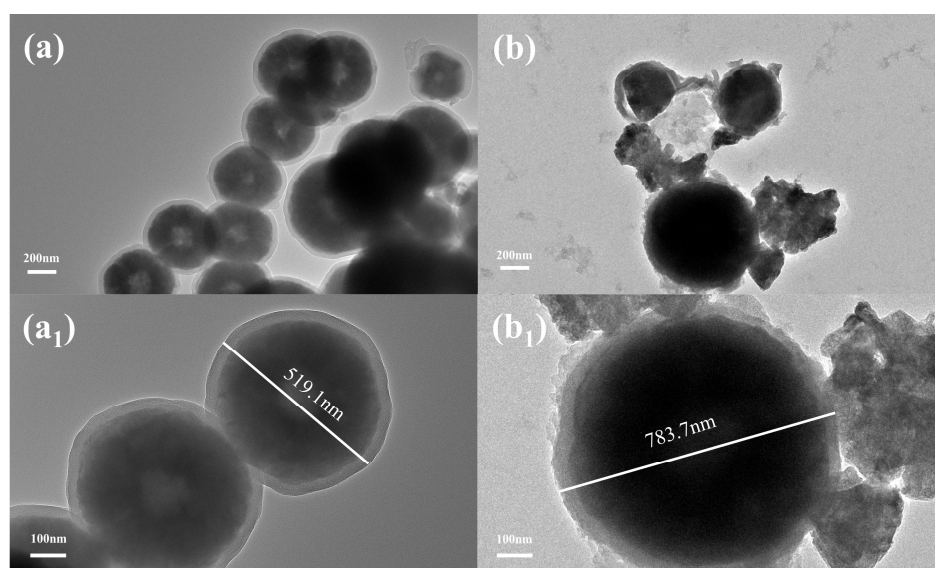


**Figure 2.** TEM images of (a)  $\text{Fe}_3\text{O}_4@\text{SiO}_2$  ((a1) enlarged TEM image of (a)) and (b)  $\text{Fe}_3\text{O}_4@\text{SiO}_2@\text{IIP}$  ((b1) enlarged TEM image of (b)).

### 3.1.2. EDS

The EDS spectra of  $\text{Fe}_3\text{O}_4@\text{SiO}_2@\text{IIP}$  before and after the adsorption of Cd(II) ions are shown in Figure 3. The presence of Fe and Si elements indicates the successful modification of  $\text{Fe}_3\text{O}_4$  nanoparticles through the silica layer. The Cd changed significantly before and after the adsorption, with the content shifting from 0.75% (Wt%) to 6.36% (Wt%), confirming the adsorption properties of  $\text{Fe}_3\text{O}_4@\text{SiO}_2@\text{IIP}$ .

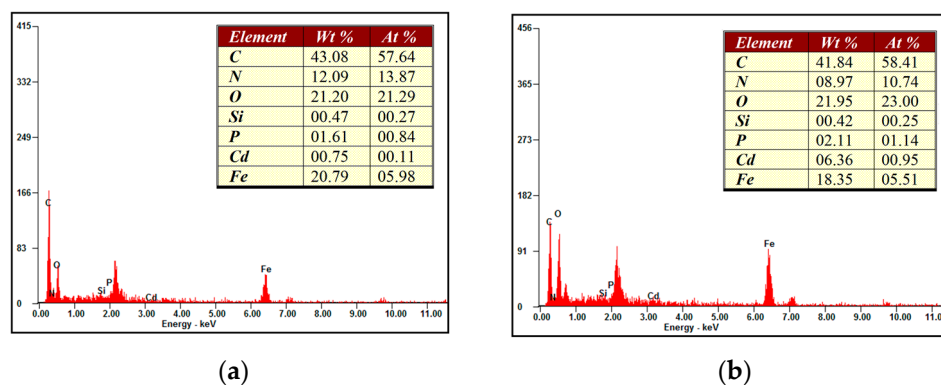


**Figure 3.** EDS spectra of (a)  $\text{Fe}_3\text{O}_4@\text{SiO}_2@\text{IIP}$  before adsorption and (b)  $\text{Fe}_3\text{O}_4@\text{SiO}_2@\text{IIP}$  after adsorption.

### 3.1.3. XRD

Phase identification was undertaken using XRD analysis. XRD patterns of the as-prepared  $\text{Fe}_3\text{O}_4$ ,  $\text{Fe}_3\text{O}_4@\text{SiO}_2$ ,  $\text{Fe}_3\text{O}_4@\text{SiO}_2@\text{IIP}$ , and  $\text{Fe}_3\text{O}_4@\text{SiO}_2@\text{NIP}$  are shown in Figure 4. Compared with  $\text{Fe}_3\text{O}_4$ ,  $\text{Fe}_3\text{O}_4@\text{SiO}_2$  showed the diffraction peaks of  $\text{Fe}_3\text{O}_4$  at angles of  $30.0^\circ$ ,  $35.3^\circ$ ,  $42.7^\circ$ ,  $53.1^\circ$ ,  $56.7^\circ$ , and  $62.3^\circ$  corresponding to the (220), (311), (400), (422), (511), and (440) crystal planes of  $\text{Fe}_3\text{O}_4$ , respectively [24,25], which confirmed the successful compounding of  $\text{Fe}_3\text{O}_4$  microspheres with  $\text{SiO}_2$ . The XRD diffraction peaks of  $\text{Fe}_3\text{O}_4@\text{SiO}_2@\text{IIP}$  and  $\text{Fe}_3\text{O}_4@\text{SiO}_2@\text{NIP}$  were almost identical and became cluttered but, again, both retained the crystal plane of  $\text{Fe}_3\text{O}_4$ , verifying the successful introduction of  $\text{Fe}_3\text{O}_4$  into the system of imprinted polymers. The detection of a characteristic peak at  $35.3^\circ$  confirmed the presence of high-crystalline  $\text{Fe}_3\text{O}_4$  in the four samples.

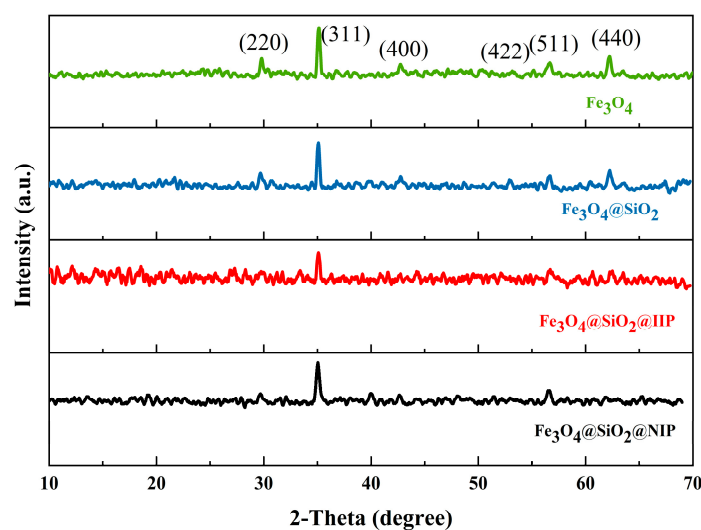


**Figure 4.** XRD patterns of  $\text{Fe}_3\text{O}_4$ ,  $\text{Fe}_3\text{O}_4@\text{SiO}_2$ ,  $\text{Fe}_3\text{O}_4@\text{SiO}_2@\text{IIP}$ , and  $\text{Fe}_3\text{O}_4@\text{SiO}_2@\text{NIP}$ .

### 3.1.4. Surface Area and Pore Size Analysis

The adsorption mechanism of the imprinted polymers was further studied in a  $\text{N}_2$  adsorption–desorption experiment. The adsorption and desorption isotherms and the

surface physical parameters are shown in Figure 5 and Table 1. The surface area was analyzed with the Brunauer–Emmett–Teller (BET) method, and the pore size distributions were determined with the Barrett–Joyner–Halenda (BJH) method. It can be seen from the figure that the shapes of the adsorption/desorption isotherms for  $\text{Fe}_3\text{O}_4@\text{SiO}_2@\text{IIP}$  could be fitted to the classic II isotherm in the IUPAC classification method, which indicates the typical characteristics of microporous materials, showing that there were two kinds of adsorption sites. The surface area and pore volume of  $\text{Fe}_3\text{O}_4@\text{SiO}_2@\text{IIP}$  were  $107.990 \text{ m}^2\cdot\text{g}^{-1}$  and  $0.235 \text{ cm}^3\cdot\text{g}^{-1}$ , respectively, higher than those of  $\text{Fe}_3\text{O}_4@\text{SiO}_2@\text{NIP}$  ( $79.455 \text{ m}^2\cdot\text{g}^{-1}$  and  $0.182 \text{ cm}^3\cdot\text{g}^{-1}$ ), which could be attributed to the specific recognition cavities for Cd(II) formed on the surface of the sorbent by the imprinting technique [26].

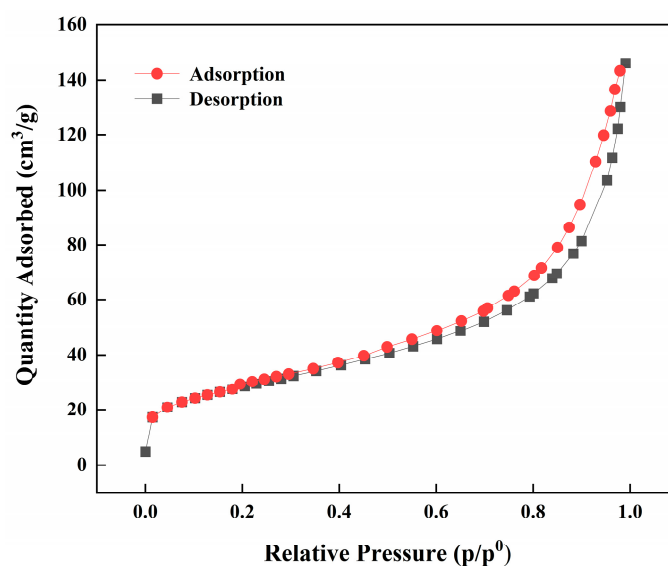


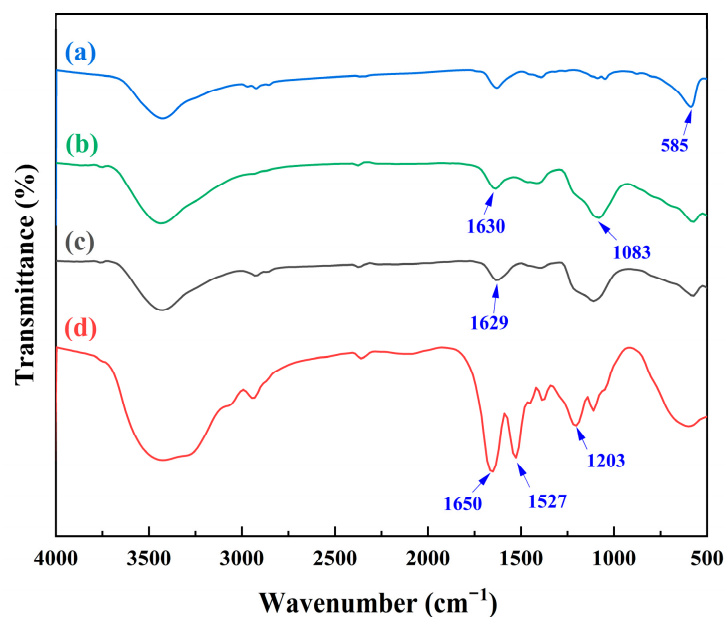
Figure 5.  $\text{N}_2$  adsorption–desorption isotherms for  $\text{Fe}_3\text{O}_4@\text{SiO}_2@\text{IIP}$ .

Table 1. Surface physical parameters of  $\text{Fe}_3\text{O}_4@\text{SiO}_2@\text{IIP}$  and  $\text{Fe}_3\text{O}_4@\text{SiO}_2@\text{NIP}$ .

Sample	Surface Area ( $\text{m}^2\cdot\text{g}^{-1}$ )	Pore Volume ( $\text{cm}^3\cdot\text{g}^{-1}$ )	Average Pore Diameter (nm)
$\text{Fe}_3\text{O}_4@\text{SiO}_2@\text{IIP}$	107.990	0.235	8.675
$\text{Fe}_3\text{O}_4@\text{SiO}_2@\text{NIP}$	79.455	0.182	8.747

### 3.1.5. FTIR Spectroscopic Analysis

The FTIR maps of the samples were swept at  $4000\sim 400 \text{ cm}^{-1}$  using the KBr infrared spectroscopy method to analyze the structures of the materials. Figure 6 shows the infrared spectra of  $\text{Fe}_3\text{O}_4$  (a),  $\text{Fe}_3\text{O}_4@\text{SiO}_2$  (b),  $\text{Fe}_3\text{O}_4@\text{SiO}_2@\text{VTMOS}$  (c), and  $\text{Fe}_3\text{O}_4@\text{SiO}_2@\text{IIP}$  (d). A strong adsorption peak at  $582 \text{ cm}^{-1}$  (a) was observed for the stretching vibration of the Fe–O band in  $\text{Fe}_3\text{O}_4$  magnetic nanoparticles [27]. The peaks for Fe–O at about  $582 \text{ cm}^{-1}$  in all the FTIR spectra (Figure 6a–d) confirmed the presence of  $\text{Fe}_3\text{O}_4$  in all the nanospheres. After TEOS treatment of the  $\text{Fe}_3\text{O}_4$ , two peaks appeared at  $1630 \text{ cm}^{-1}$  and  $1083 \text{ cm}^{-1}$  (b). The former was due to the existence of O–H and the latter was the stretching vibration of Si–O, which verified that the  $\text{Fe}_3\text{O}_4$  nanospheres were coated with  $\text{SiO}_2$  shells [28]. The peak at  $1629 \text{ cm}^{-1}$  (c) was caused by C=C stretching vibration. This proved that the double bond was successfully grafted onto the surface of  $\text{Fe}_3\text{O}_4@\text{SiO}_2$  [29].



**Figure 6.** FTIR spectra of  $\text{Fe}_3\text{O}_4$  (a),  $\text{Fe}_3\text{O}_4@\text{SiO}_2$  (b),  $\text{Fe}_3\text{O}_4@\text{SiO}_2@\text{VTMOS}$  (c), and  $\text{Fe}_3\text{O}_4@\text{SiO}_2@\text{IIP}$  (d).

The new peaks appearing at 1650 and 1203  $\text{cm}^{-1}$  (d) were assigned to the characteristic peaks of C=O and P=O bonds [30], respectively. This confirmed the abundant presence of carboxyl groups and phosphonic groups on the  $\text{Fe}_3\text{O}_4@\text{SiO}_2@\text{IIP}$  surfaces. In addition, the characteristic peak of the NH bond at 1527  $\text{cm}^{-1}$  revealed the presence of MBA as crosslinker [31]. The appearance of these peaks indicated that the PBTCA was successfully grafted onto the  $\text{Fe}_3\text{O}_4@\text{SiO}_2@\text{VTMOS}$  surface. These results demonstrated that  $\text{Fe}_3\text{O}_4@\text{SiO}_2@\text{IIP}$  was successfully synthesized via surface-imprinting polymerization.

### 3.1.6. Magnetic Separation Performance

As shown in Figure 7, the hysteresis regression curves of the three materials had similar shapes and all passed through the origin, indicating their superparamagnetic nature and strong magnetic responsiveness to magnetic fields. This responsiveness is beneficial for magnetic separation purposes. The saturation magnetization intensity of  $\text{Fe}_3\text{O}_4$  at room temperature was found to be 66.79 emu/g, while that of  $\text{Fe}_3\text{O}_4@\text{SiO}_2$  was reduced to 63.89 emu/g. The observed reduction in saturation magnetization intensity could be attributed to the presence of a  $\text{SiO}_2$  layer on the surface of the  $\text{Fe}_3\text{O}_4$  nanoparticles. This layer resulted in a decrease in the mass fraction of the magnetic components. The saturation magnetization intensity of  $\text{Fe}_3\text{O}_4@\text{SiO}_2@\text{IIP}$  was found to be significantly lower than that of bare  $\text{Fe}_3\text{O}_4$  (15.02 emu/g). This reduction in saturation magnetization intensity can be attributed to the shielding effect of the polymer shell on the surface of the  $\text{Fe}_3\text{O}_4$  [27]. As shown in the inset image in Figure 5,  $\text{Fe}_3\text{O}_4@\text{SiO}_2@\text{IIP}$  could be completely separated from the solution by an external magnetic field. The black dispersions after magnetic separation could become clear and transparent in a very short time (about 25 s). These results confirmed that the obtained  $\text{Fe}_3\text{O}_4@\text{SiO}_2@\text{IIP}$  had outstanding magnetic properties and could be used for fast magnetic separation.

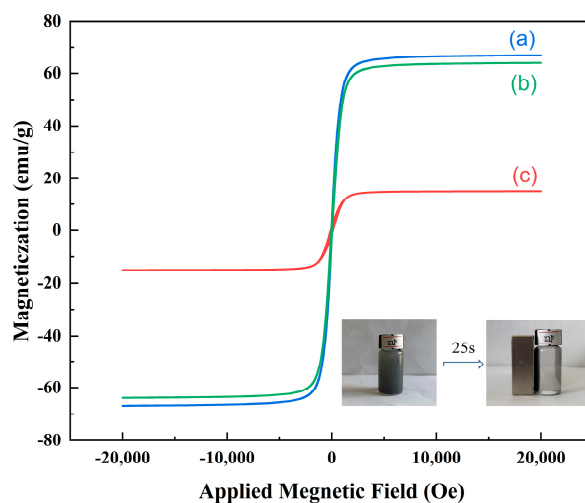


**Figure 7.** The hysteresis curves for  $\text{Fe}_3\text{O}_4$  (a),  $\text{Fe}_3\text{O}_4@\text{SiO}_2$  (b), and  $\text{Fe}_3\text{O}_4@\text{SiO}_2@\text{IIP}$  (c).

### 3.1.7. Thermal Stability Analysis

The thermal stability of the magnetic Cd(II) ion-imprinted material was studied with TGA in the range of  $25\text{ }^\circ\text{C}$ – $800\text{ }^\circ\text{C}$  at a heating rate of  $10\text{ }^\circ\text{C min}^{-1}$  under a nitrogen atmosphere.  $\text{Fe}_3\text{O}_4$  (Figure 8a) and  $\text{Fe}_3\text{O}_4@\text{SiO}_2$  (Figure 8b) underwent a first drop at  $150\text{ }^\circ\text{C}$ , but it was not significant and probably due to the evaporation of water.  $\text{Fe}_3\text{O}_4$  and  $\text{Fe}_3\text{O}_4@\text{SiO}_2$  demonstrated weight losses of 23.5% and 8.22%, respectively, as the temperature increased from  $25\text{ }^\circ\text{C}$  to  $800\text{ }^\circ\text{C}$ . This was attributed to the successful coating of  $\text{SiO}_2$  on the surface of the  $\text{Fe}_3\text{O}_4$ . The modification of  $\text{SiO}_2$  resulted in an improvement in the thermal stability of  $\text{Fe}_3\text{O}_4@\text{SiO}_2$ . For  $\text{Fe}_3\text{O}_4@\text{SiO}_2@\text{IIP}$  (Figure 8c), the first weight loss was about 17.1% and occurred as the temperature changed from room temperature to  $150\text{ }^\circ\text{C}$ ; it was attributed to the loss of the adsorbed water in the polymers, which was not eliminated during the drying process. When the temperature increased from 150 to  $260\text{ }^\circ\text{C}$ , the thermal weight loss was minimal, indicating that the imprinted material could remain stable below  $260\text{ }^\circ\text{C}$ . However, the weight loss was significant in the temperature range from 260 to  $480\text{ }^\circ\text{C}$  at about 45.9%, which may have been due to the decomposition of the imprinted polymer layer on the surface of the  $\text{Fe}_3\text{O}_4@\text{SiO}_2$ . The results showed that the prepared magnetic Cd(II) imprinted material had good thermal stability at temperatures below  $260\text{ }^\circ\text{C}$ .

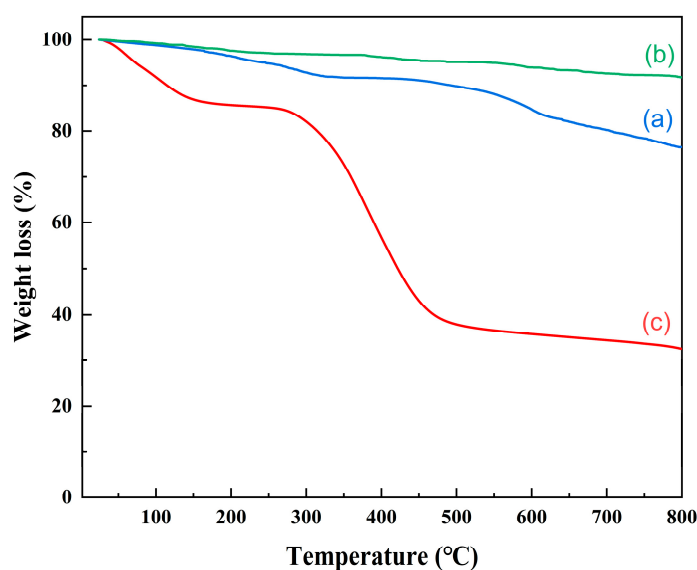


**Figure 8.** TG curves for  $\text{Fe}_3\text{O}_4$  (a),  $\text{Fe}_3\text{O}_4@\text{SiO}_2$  (b), and  $\text{Fe}_3\text{O}_4@\text{SiO}_2@\text{IIP}$  (c).

### 3.2. Effect of pH on Adsorption

The pH of a solution has a significant impact on the adsorption of metal ions as it affects both the morphology of the ions in the aqueous solution and the charge distribution on the surface of the adsorbent material [32]. Given that Cd(II) ions hydrolyze when  $\text{pH} > 8.0$ , the effects of different pH values on the adsorption properties of Cd(II) were studied at room temperature under the conditions of a Cd(II) concentration of  $50 \text{ mg}\cdot\text{L}^{-1}$  and pH values in the range of 2.0–8.0. The results are shown in Figure 9. The adsorption capacity of the  $\text{Fe}_3\text{O}_4@\text{SiO}_2@\text{IIP}$  for Cd(II) increased gradually with the increase in solution pH and reached the maximum value of  $13.88 \text{ mg}\cdot\text{g}^{-1}$  at the solution  $\text{pH} = 6.0$ . This may have been due to the high protonation of the imprinted polymer surface groups in the form of  $-\text{COOH}$  at low pH conditions, which caused severe repulsion from Cd(II) in solution. As the pH rose, the degree of protonation on the adsorbent surface gradually decreased, making it easier for Cd(II) ions to bind with carboxyl and phosphate groups on the surface of the adsorbent, thereby enhancing the chelation of Cd(II). When  $\text{pH} > 6.0$ , the adsorption capacity decreased with the increasing pH. This may have been due to the fact that it was Cd(II) that was hydrolyzed and precipitated, and some of the Cd(II) in the system was hydrolyzed to  $\text{Cd}(\text{OH})^+$ , reducing the repulsive forces between them and resulting in a lower concentration of free Cd(II) and, thus, lower adsorption [33,34]. Therefore, a pH value of 6.0 in aqueous solution was selected as the optimal pH for the subsequent experiments.

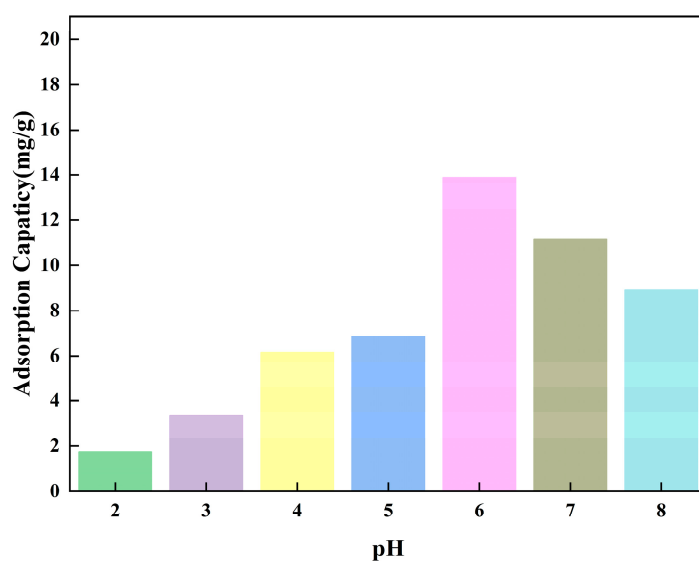
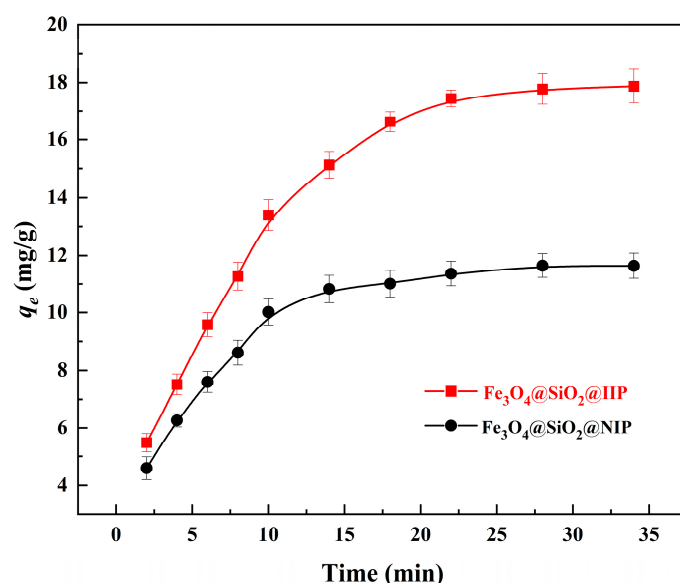


Figure 9. Effect of pH on the adsorption capacity of  $\text{Fe}_3\text{O}_4@\text{SiO}_2@\text{IIP}$ .

### 3.3. Adsorption Kinetics

The adsorption kinetics for Cd(II) were assessed by measuring the adsorption equilibrium time for the adsorbent under conditions of an initial Cd(II) concentration of  $50 \text{ mg}\cdot\text{L}^{-1}$ ,  $\text{pH} = 6.0$ , and a temperature of  $25^\circ\text{C}$ . As shown in Figure 10,  $\text{Fe}_3\text{O}_4@\text{SiO}_2@\text{NIP}$  obtained adsorption equilibrium faster than  $\text{Fe}_3\text{O}_4@\text{SiO}_2@\text{IIP}$  but with a reduced adsorption capacity.  $\text{Fe}_3\text{O}_4@\text{SiO}_2@\text{NIP}$  had a lower uptake rate due to the smaller surface area and reached equilibrium earlier compared to  $\text{Fe}_3\text{O}_4@\text{SiO}_2@\text{IIP}$ . Owing to the presence of template Cd(II) ions,  $\text{Fe}_3\text{O}_4@\text{SiO}_2@\text{IIP}$  had more adsorption sites than  $\text{Fe}_3\text{O}_4@\text{SiO}_2@\text{NIP}$ , resulting in a higher adsorption capacity ( $18.21 \text{ mg}\cdot\text{g}^{-1}$ ) and a longer time (22 min) being required to reach adsorption saturation.



**Figure 10.** Effects of time on Cd<sup>2+</sup> adsorption on Fe<sub>3</sub>O<sub>4</sub>@SiO<sub>2</sub>@IIP and Fe<sub>3</sub>O<sub>4</sub>@SiO<sub>2</sub>@NIP.

To further investigate the kinetics of the adsorption mechanism of the imprinted materials, pseudo-first-order kinetics (Equation (6)), pseudo-second-order kinetics (Equation (7)), and Weber–Morris kinetic models (Equation (8)) were used for linear fitting of the data [35]:

$$\ln(q_e - q_t) = \ln q_e - k_1 t \quad (6)$$

$$\frac{t}{q_t} = \frac{1}{k_2 q_e^2} + \frac{1}{q_e} t \quad (7)$$

$$q_t = K_i t^{0.5} + C \quad (8)$$

where  $q_t$  (mg·g<sup>-1</sup>) and  $q_e$  (mg·g<sup>-1</sup>) are the adsorption capacities of Cd(II) at time  $t$  (min) and equilibrium, respectively;  $k_1$  (min<sup>-1</sup>) is the rate constant of the first-order model;  $k_2$  (g·min<sup>-1</sup>·mg<sup>-1</sup>) is the rate constant for the pseudo-second-order model at equilibrium;  $K_i$  (mg·g<sup>-1</sup>·min<sup>0.5</sup>) indicates the rate constants for the Weber intra-particle diffusion model; and  $C$  gives the boundary layer thickness.

Figure 11a presents the plots of the pseudo-first-order and pseudo-second-order kinetic models for the adsorption of Cd(II) ions, and the parameters of the two kinetic models are given in Table 2. The results showed that, compared with the pseudo-first-order kinetic model, the pseudo-second-order kinetic model was more suitable for the experimental data for Fe<sub>3</sub>O<sub>4</sub>@SiO<sub>2</sub>@IIP and Fe<sub>3</sub>O<sub>4</sub>@SiO<sub>2</sub>@NIP in relation to Cd(II), and the correlation coefficients ( $R_2^2$ ) were higher than 0.99. The pseudo-first-order kinetic model suggested that the adsorption process proceeded via diffusion of metal ions through the boundary layer on the adsorbent surface and that this adsorption process was controlled by the diffusion step, while the pseudo-second-order model assumed that the adsorption process was controlled by a chemisorption mechanism that involved electron sharing or electron transfer between the adsorbent and the adsorbate [36]. In general, the pseudo-second-order model could better explain the adsorption behavior because it was set across the whole range of the adsorption equilibrium time. Thus, it can be speculated that the adsorption of Cd(II) on Fe<sub>3</sub>O<sub>4</sub>@SiO<sub>2</sub>@IIP and Fe<sub>3</sub>O<sub>4</sub>@SiO<sub>2</sub>@NIP occurs via chemical adsorption.

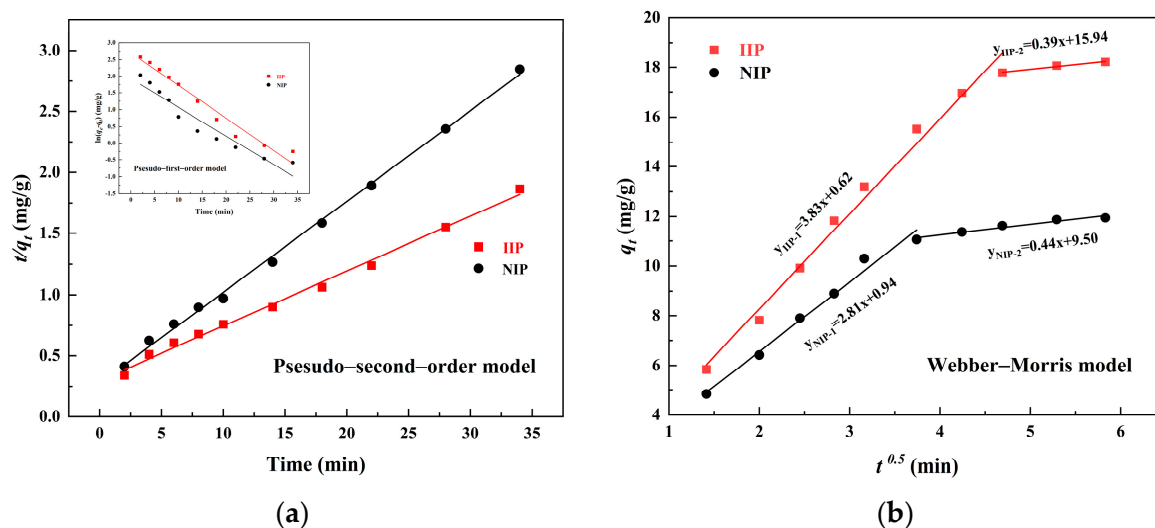


**Figure 11.** Pseudo-second-order kinetic model (the inset shows the pseudo-first-order kinetic model) (a) and Weber–Morris intra-particle diffusion model (b).

**Table 2.** The adsorption kinetic parameters for IIP and NIP.

Adsorption	$q_{e, \text{exp}}$	Pseudo-First-Order Kinetic Model			Pseudo-Second-Order Kinetic Model		
		$k_1$	$q_{e, \text{cal}}$	$R_1^2$	$k_2$	$q_{e, \text{cal}}$	$R_2^2$
IIP	18.21	0.2245	14.90	0.9658	0.0068	22.30	0.9945
NIP	11.94	0.1971	6.86	0.9264	0.0199	13.46	0.9978

The Weber–Morris model was introduced to further investigate the mechanism of the adsorption process. As shown in Figure 11b, the adsorption process could be divided into two stages by the Weber–Morris model. In the first stage, the diffusion rate constant  $K_1$  values for IIP and NIP were 3.83 and 2.81  $\text{mg} \cdot \text{g}^{-1} \cdot \text{min}^{0.5}$ , respectively. This stage was attributed to the introduction of the template ions such that the IIP had more imprinted sites than the NIP, resulting in a higher diffusion rate constant for the IIP ( $K_{\text{IIP-1}}$ ) than for the NIP ( $K_{\text{NIP-1}}$ ) at this stage. In the second stage, both the IIP and NIP surfaces were almost saturated with adsorption after the first stage of rapid adsorption. This resulted in very low diffusion rate constants for IIP ( $K_{\text{IIP-2}}$ ) and NIP ( $K_{\text{NIP-2}}$ ) in the second stage of 0.39 and 0.44  $\text{mg} \cdot \text{g}^{-1} \cdot \text{min}^{0.5}$ , respectively [37].

### 3.4. Adsorption Isotherms

Figure 12 shows the room temperature Cd(II) sorption isotherms for  $\text{Fe}_3\text{O}_4@ \text{SiO}_2@ \text{IIP}$  and  $\text{Fe}_3\text{O}_4@ \text{SiO}_2@ \text{NIP}$  (at 25 °C and pH = 6.0 with initial Cd(II) concentration in the range of 25–205  $\text{mg} \cdot \text{L}^{-1}$ ). At the corresponding initial concentrations, the adsorption capacity of  $\text{Fe}_3\text{O}_4@ \text{SiO}_2@ \text{NIP}$  was clearly lower than that of  $\text{Fe}_3\text{O}_4@ \text{SiO}_2@ \text{IIP}$ . This can be explained by the specific effect: the specific adsorption sites present on the surface of  $\text{Fe}_3\text{O}_4@ \text{SiO}_2@ \text{IIP}$  were complementary to the template in terms of size and coordination geometries, which was favorable for the binding of Cd(II) with the recognition sites.

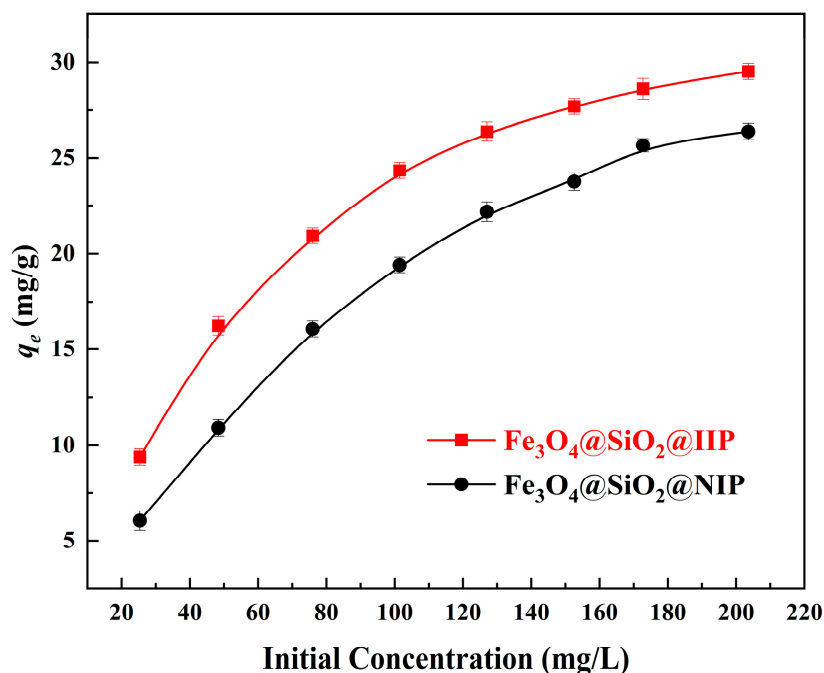


**Figure 12.** Effects of the initial concentration of Cd(II) on the adsorption capacity of Fe<sub>3</sub>O<sub>4</sub>@SiO<sub>2</sub>@IIP and Fe<sub>3</sub>O<sub>4</sub>@SiO<sub>2</sub>@NIP.

The Langmuir isotherm model, Freundlich isotherm model, and Scatchard model were fitted to the data to further investigate the adsorption mechanism of the adsorbent. The equations for the models are shown in Equations (9)–(11) [38]:

$$\frac{c_e}{q_e} = \frac{1}{q_m K_L} + \frac{c_e}{q_m} \quad (9)$$

$$\log q_e = \log K_F + \frac{1}{n} \log c_e \quad (10)$$

$$\frac{q_e}{c_e} = \frac{q_m - q_e}{K_s} \quad (11)$$

where  $c_e$  ( $\text{mg}\cdot\text{L}^{-1}$ ) indicates the equilibrium concentrations of Cd(II) ions in solution,  $q_m$  ( $\text{mg}\cdot\text{g}^{-1}$ ) is the maximum adsorption capacity of the Cd(II) ion,  $K_L$  ( $\text{L}\cdot\text{g}^{-1}$ ) is the Langmuir model constant,  $K_F$  and  $n$  are the Freundlich model constants, and  $K_s$  is the equilibrium dissociation constant at the binding sites in the Scatchard model.

The fitting results for the two models are shown in Figure 13, and the adsorption constants calculated from the corresponding isotherms with the correlation coefficients are given in Table 3. As shown in the table, the adsorption of Cd(II) onto Fe<sub>3</sub>O<sub>4</sub>@SiO<sub>2</sub>@IIP and Fe<sub>3</sub>O<sub>4</sub>@SiO<sub>2</sub>@NIP was well-fitted by the Langmuir model with a higher  $R^2$  (0.9988 and 0.9859). The consistency between the adsorption data and the Langmuir isotherm could be explained by the fact that the adsorption sites on the adsorbent surface were homogeneous, resulting in monolayer binding. Moreover, the Freundlich constant  $1/n$  was less than 1, indicating a favorable process [11].

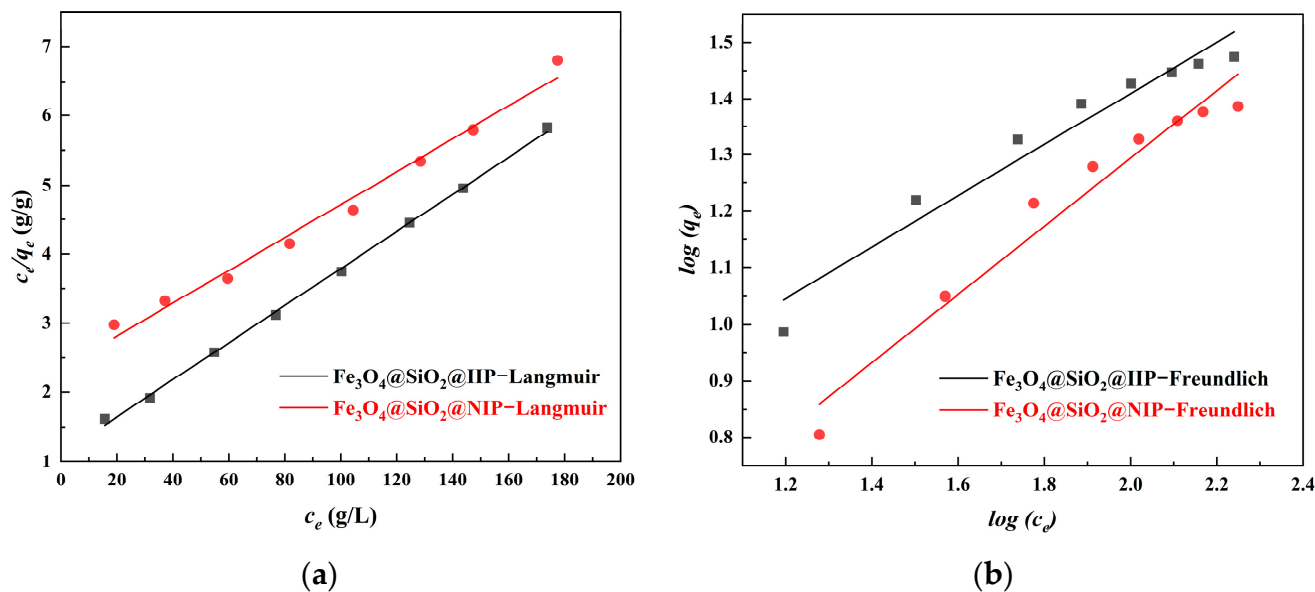


**Figure 13.** Isotherm model fitting curves for Fe<sub>3</sub>O<sub>4</sub>@SiO<sub>2</sub>@IIP and Fe<sub>3</sub>O<sub>4</sub>@SiO<sub>2</sub>@NIP. (a) Langmuir model and (b) Freundlich model.

**Table 3.** Isotherm model parameters used for the Fe<sub>3</sub>O<sub>4</sub>@SiO<sub>2</sub>@IIP and Fe<sub>3</sub>O<sub>4</sub>@SiO<sub>2</sub>@NIP.

Adsorbents	$q_{e, \text{exp}}$	Langmuir			Freundlich		
		$K_L$	$q_m$	$R^2$	$n$	$K_F$	$R^2$
Fe <sub>3</sub> O <sub>4</sub> @SiO <sub>2</sub> @IIP	29.82	0.02429	37.24	0.9988	2.199	3.162	0.9501
Fe <sub>3</sub> O <sub>4</sub> @SiO <sub>2</sub> @NIP	24.35	0.01018	42.03	0.9859	1.659	1.225	0.9592

In the Scatchard model (Figure 14), the process of adsorption of Cd(II) on Fe<sub>3</sub>O<sub>4</sub>@SiO<sub>2</sub>@IIP exhibited two different linear relationships at different concentrations. This means that there were two types of Cd(II) binding sites on the Fe<sub>3</sub>O<sub>4</sub>@SiO<sub>2</sub>@IIP [39]. This was consistent with the results of the BET analysis. The first were non-specific binding sites with strong affinity formed by Cd(II) and two functional groups (-OH)<sub>2</sub>PO and -COOH in the functional monomer PBTCA, and the others were specific imprinted cavities formed on the surface of the imprinted polymer through the imprinting polymerization reaction. In contrast, for Fe<sub>3</sub>O<sub>4</sub>@SiO<sub>2</sub>@NIP,  $q_e$  showed a linear relationship with  $q_e/c_e$ , indicating that only non-specific binding sites existed on the Fe<sub>3</sub>O<sub>4</sub>@SiO<sub>2</sub>@NIP due to the fact that no template ion was introduced during the preparation of the Fe<sub>3</sub>O<sub>4</sub>@SiO<sub>2</sub>@NIP, resulting in an inability to generate imprinting cavities. Based on the intercept and slope of the fitted line, the dissociation constant ( $K_s$ ) and the maximum adsorption amount ( $q_m$ ) for the affinity site could be obtained, and the results are shown in Table 4; the smaller the  $K_s$ , the higher the affinity is [40]. Notably, the fitted  $K_s$  values for each segment of the Fe<sub>3</sub>O<sub>4</sub>@SiO<sub>2</sub>@IIP (51.12 and 35.00) were smaller than that for the Fe<sub>3</sub>O<sub>4</sub>@SiO<sub>2</sub>@NIP (93.28), which proved that Fe<sub>3</sub>O<sub>4</sub>@SiO<sub>2</sub>@IIP had a stronger affinity for Cd(II) than Fe<sub>3</sub>O<sub>4</sub>@SiO<sub>2</sub>@NIP, and thus its adsorption capacity was higher than that of Fe<sub>3</sub>O<sub>4</sub>@SiO<sub>2</sub>@NIP.

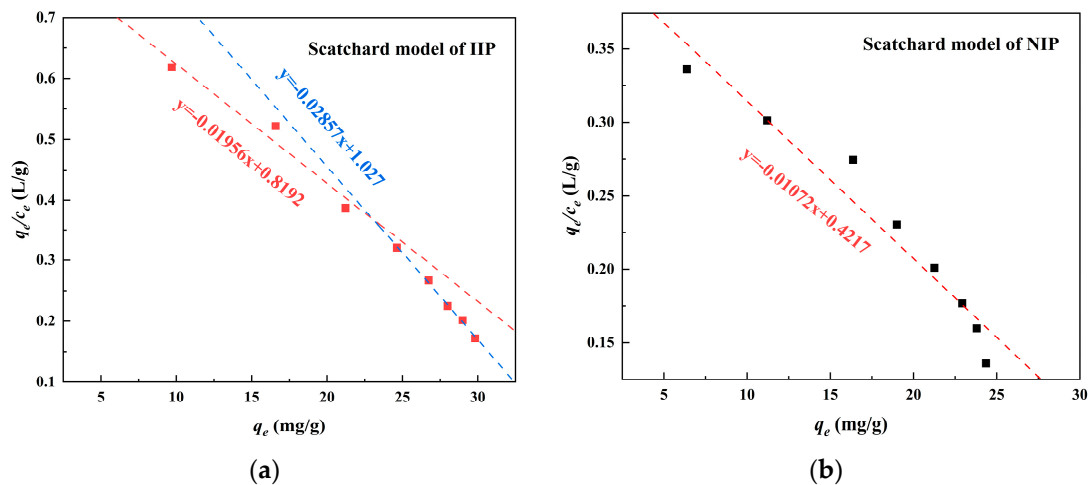


Figure 14. Scatchard model fitting for the IIP (a) and NIP (b).

Table 4. Parameters for the Scatchard model.

Adsorbents	$q_{e, \text{exp}}$ ( $\text{mg}\cdot\text{g}^{-1}$ )	$K_s$ ( $\text{mg}\cdot\text{L}^{-1}$ )	$q_m$ ( $\text{mg}\cdot\text{g}^{-1}$ )	$R^2$
$\text{Fe}_3\text{O}_4@\text{SiO}_2@\text{IIP}$	29.82	51.12	41.88	0.9583
		35.00	35.94	0.9966
$\text{Fe}_3\text{O}_4@\text{SiO}_2@\text{NIP}$	24.35	93.28	39.34	0.9452

### 3.5. Adsorption Thermodynamic

The effect of temperature on the adsorption equilibrium of Cd(II) for  $\text{Fe}_3\text{O}_4@\text{SiO}_2@\text{IIP}$  and  $\text{Fe}_3\text{O}_4@\text{SiO}_2@\text{NIP}$  (solution pH = 6.0, initial Cd(II) concentration of  $50 \text{ mg}\cdot\text{L}^{-1}$ , and temperature range of  $25\text{ }^\circ\text{C}$ – $45\text{ }^\circ\text{C}$ ) was also investigated. Figure 15 shows the influence curve for temperature in relation to the adsorption capacity. The results showed that an increase in temperature was favorable for Cd(II) adsorption. Higher temperatures may increase the adsorbent pore size, allowing more Cd(II) to diffuse into the adsorbent. Furthermore, higher temperatures are more conducive to the diffusion of Cd(II) into the adsorbent system and its binding to the binding sites on the adsorbent surface.

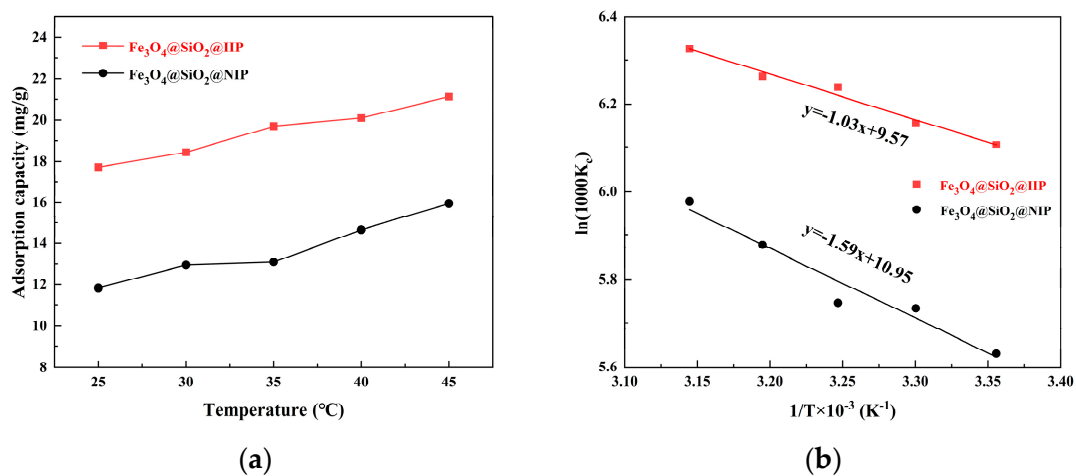


Figure 15. Effect of temperature on the adsorption (a) and plot of  $\ln K_c$  versus  $1/T$  (b).

To further explore the thermodynamic mechanism of the adsorption process, the Gibbs free energy equation (Equation (12)) and the Van't Hoff equation (Equation (13)) were introduced as follows [41]:

$$\Delta G = -RT\ln(1000K_c) \quad (12)$$

$$\ln K_c = -\frac{\Delta H}{RT} + \frac{\Delta S}{R} \quad (13)$$

where  $R$  is the universal gas constant ( $8.314 \text{ J mol}^{-1} \text{ K}^{-1}$ ),  $T$  is the absolute temperature (K), and  $K_c$  is the equilibrium constant ( $K_c = \frac{q_e}{c_e}$ ). The value of  $\Delta G$  was calculated directly from the above relations, and the slope and the intercept of  $\ln K_c$  versus  $1/T$  were used to calculate the values of  $\Delta H$  and  $\Delta S$ .

As shown in Table 5, the  $\Delta G$  had negative values at different temperatures, indicating that the sorption of Cd(II) on  $\text{Fe}_3\text{O}_4@\text{SiO}_2@\text{IIP}$  was spontaneous [40,42]. In addition, the  $\Delta G$  decreased with the increase in temperature, indicating that a higher temperature was more favorable for the sorption process. On the other hand, the positive values for the  $\Delta H$  suggested the endothermic nature of Cd(II) adsorption [43,44], which could have been due to some energy consumption for overcoming this potential barrier when the adsorption occurred near the imprinted adsorbent surface. It is worth noting that the  $\Delta H$  value calculated in this work ( $8.56 \text{ kJ}\cdot\text{mol}^{-1}$ ) lay between the energy level of the electrostatic interactions of a Cd(II) complex ( $<4 \text{ kJ}\cdot\text{mol}^{-1}$ ) and that of a hydrogen bond ( $20.92 \text{ kJ}\cdot\text{mol}^{-1}$ ) [45]. When  $\text{Fe}_3\text{O}_4@\text{SiO}_2@\text{IIP}$  reached adsorption saturation, increasing the temperature was favorable for its adsorption, and the increment in the maximum adsorption was related to the van der Waals force according to the value of the  $\Delta H$ . For the  $\Delta S$ , its positive value indicated that the higher temperature increased the solid–liquid interfacial irregularity of the adsorption process, while the relatively low entropy value indicated that the process maintained the relative regularity of Cd(II) on the polymer surface [44]. To conclude, the Cd(II) adsorption on the  $\text{Fe}_3\text{O}_4@\text{SiO}_2@\text{IIP}$  surface was predominantly an endothermic, entropy-increasing process.

**Table 5.** Thermodynamic parameters for Cd(II) adsorption.

Adsorbent	Temperature (K)	$\Delta G$ ( $\text{kJ}\cdot\text{mol}^{-1}$ )	$\Delta H$ ( $\text{kJ}\cdot\text{mol}^{-1}$ )	$\Delta S$ ( $\text{J}\cdot\text{mol}^{-1}\cdot\text{K}^{-1}$ )
$\text{Fe}_3\text{O}_4@\text{SiO}_2@\text{IIP}$	298	−15.13	8.56	79.56
	303	−15.51		
	308	−15.97		
	313	−16.03		
	318	−16.72		
$\text{Fe}_3\text{O}_4@\text{SiO}_2@\text{NIP}$	298	−13.95	13.22	91.04
	303	−14.44		
	308	−14.71		
	313	−15.30		
	318	−15.81		

### 3.6. Selectivity Study and Reusability

In order to evaluate the selectivity of  $\text{Fe}_3\text{O}_4@\text{SiO}_2@\text{IIP}$  and  $\text{Fe}_3\text{O}_4@\text{SiO}_2@\text{NIP}$  for Cd(II), Zn(II), Ni(II), and Co(II) were selected as competing ions for selective adsorption experiments, and the results are shown in Figure 16 and Table 6. It can be seen that the adsorption selectivity of  $\text{Fe}_3\text{O}_4@\text{SiO}_2@\text{IIP}$  for Cd(II) was much higher than that of the other metal ions, with a  $D_{\text{Cd(II)}}$  of  $643.30 \text{ mL}\cdot\text{g}^{-1}$  and a  $k_{\text{Cd(II)}/\text{Co(II)}}$  of up to 16.58 for  $\text{Fe}_3\text{O}_4@\text{SiO}_2@\text{IIP}$ . However, the  $D_{\text{Cd(II)}}$  value for  $\text{Fe}_3\text{O}_4@\text{SiO}_2@\text{NIP}$  was smaller than those of  $D_{\text{Ni(II)}}$  and  $D_{\text{Co(II)}}$ . This indicated that the phosphonate and carboxyl groups in the

functional monomers had their own affinities, and the order of affinity for these ions was: Ni(II) > Co(II) > Cd(II) > Zn(II).

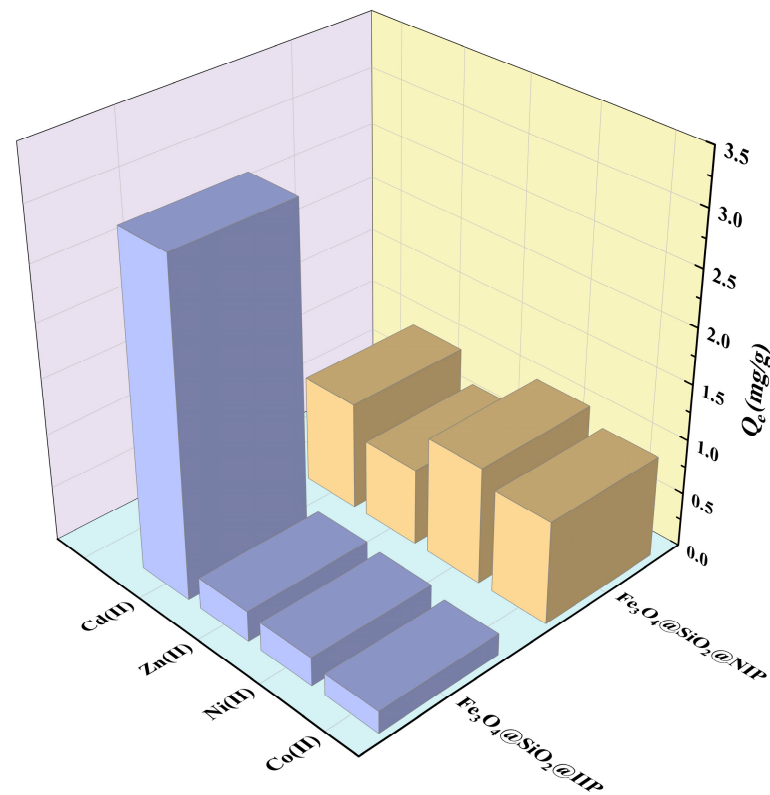


**Figure 16.** Selective adsorption of Fe<sub>3</sub>O<sub>4</sub>@SiO<sub>2</sub>@IIP and Fe<sub>3</sub>O<sub>4</sub>@SiO<sub>2</sub>@NIP.

**Table 6.** Selectivity parameters for Fe<sub>3</sub>O<sub>4</sub>@SiO<sub>2</sub>@IIP and Fe<sub>3</sub>O<sub>4</sub>@SiO<sub>2</sub>@NIP.

Metal Ion	Fe <sub>3</sub> O <sub>4</sub> @SiO <sub>2</sub> @IIP			Fe <sub>3</sub> O <sub>4</sub> @SiO <sub>2</sub> @NIP			<i>k'</i>
	<i>q<sub>e</sub></i> (mg·g <sup>-1</sup> )	<i>D</i> (mL·g <sup>-1</sup> )	<i>k</i>	<i>q<sub>e</sub></i> (mg·g <sup>-1</sup> )	<i>D</i> (mL·g <sup>-1</sup> )	<i>k</i>	
Cd(II)	3.02	643.30		0.98	172.06		
Zn(II)	0.28	54.12	11.89	0.70	139.82	1.23	9.67
Ni(II)	0.26	51.78	12.42	1.07	230.34	0.75	16.56
Co(II)	0.20	38.81	16.58	0.93	197.39	0.87	19.06

To explore the mechanism underlying this high selectivity, the binding energy of Cd(II) and other metals to PBTCAs was calculated with the DFT method. As shown in Figure 17, the descending order of the binding energies of PBTCAs with these metal ions was Ni(II), Co(II), Cd(II), and Zn(II), and the calculated results were consistent with the selective adsorption capacity of Fe<sub>3</sub>O<sub>4</sub>@SiO<sub>2</sub>@NIP. The results showed that Fe<sub>3</sub>O<sub>4</sub>@SiO<sub>2</sub>@IIP was made specific by the imprinting technology, and this specificity dominated the selective adsorption of Cd(II) from other interfering metal ions.

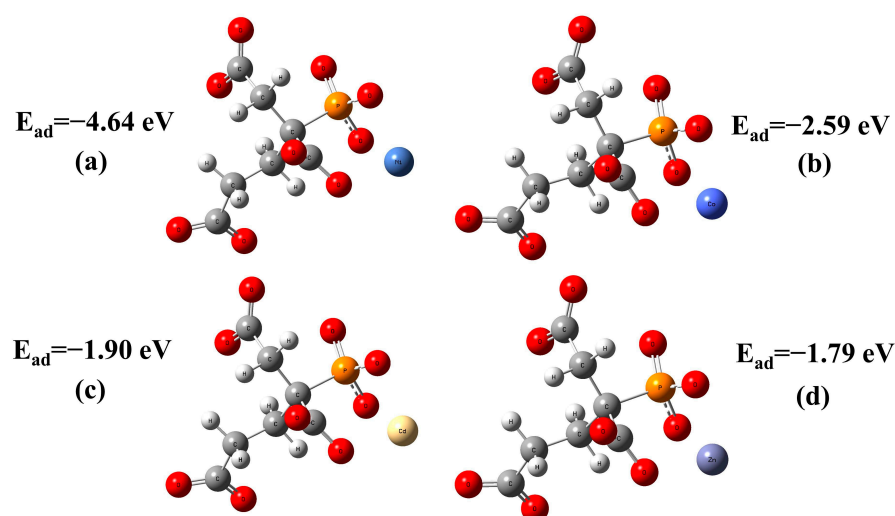


**Figure 17.** Binding energies of different ions to PTBCA: (a) PTBCA-Ni(II), (b) PTBCA-Co(II), (c) PTBCA-Cd(II), and (d) PTBCA-Zn(II).

To investigate the stability and reusability of  $\text{Fe}_3\text{O}_4@\text{SiO}_2@\text{IIP}$ , six adsorption–desorption experiments were carried out with  $50 \text{ mg}\cdot\text{L}^{-1}$  Cd(II) solution using  $2 \text{ mg}\cdot\text{L}^{-1}$  HCl aqueous solution as eluent, as shown in Figure 18. Compared to the initial cycle, the adsorption capacity of  $\text{Fe}_3\text{O}_4@\text{SiO}_2@\text{IIP}$  only decreased by 7.32% for Cd(II), revealing the good regeneration capacity of  $\text{Fe}_3\text{O}_4@\text{SiO}_2@\text{IIP}$ .

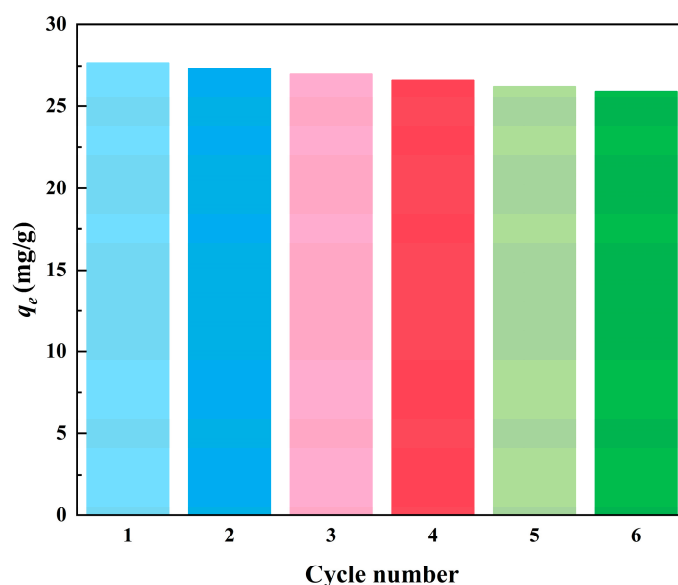


**Figure 18.** Regeneration performance of  $\text{Fe}_3\text{O}_4@\text{SiO}_2@\text{IIP}$  in six adsorption-desorption cycles.

### 3.7. Selective Adsorption Mechanism

XPS analysis was carried out before and after the adsorption of Cd(II) by the imprinted polymer to further investigate the mechanism of adsorption of Cd(II) on  $\text{Fe}_3\text{O}_4@\text{SiO}_2@\text{IIP}$ , and the XPS spectrum of the imprinted polymer after Cd(II) adsorption is shown in Figure 19a. The new characteristic peaks at 412.42 and 405.09 eV in the survey spectra were attributed to Cd 3d<sub>3/2</sub> and Cd 3d<sub>5/2</sub>, respectively. The high-resolution XPS spectrum of Cd(II) is shown in Figure 19b, further indicating the imprinted polymer's adsorption capacity for Cd(II). Deconvolution analysis of the O1s and N1s spectra was performed to examine the interactions between Cd(II) and the functional groups on  $\text{Fe}_3\text{O}_4@\text{SiO}_2@\text{IIP}$ . Before Cd(II) adsorption, the O1s spectrum (Figure 19c) could be deconvoluted into two

individual peaks with binding energies of 531.79 and 530.83 eV, which were ascribed to O atoms of the -COOH and -PO<sub>3</sub>H<sub>2</sub> groups in the functional monomer PBTCA, respectively [46]. After Cd(II) adsorption, the O1s peaks shifted to higher binding energies of 532.23 and 531.03 eV, respectively. These shifts were caused by the empty orbitals of the cadmium atom sharing the electron cloud of the oxygen atom [19]. However, as shown in Figure 19d, the change in the binding energy of N1s was significantly less than 0.2 eV when Fe<sub>3</sub>O<sub>4</sub>@SiO<sub>2</sub>@IIP adsorbed Cd(II); therefore, the N atom was considered not to be involved in coordination. The results showed that the O atoms of the carboxylic acid groups and the phosphonic acid groups in PBTCA play a critical role in the high capture capacity for Cd(II).

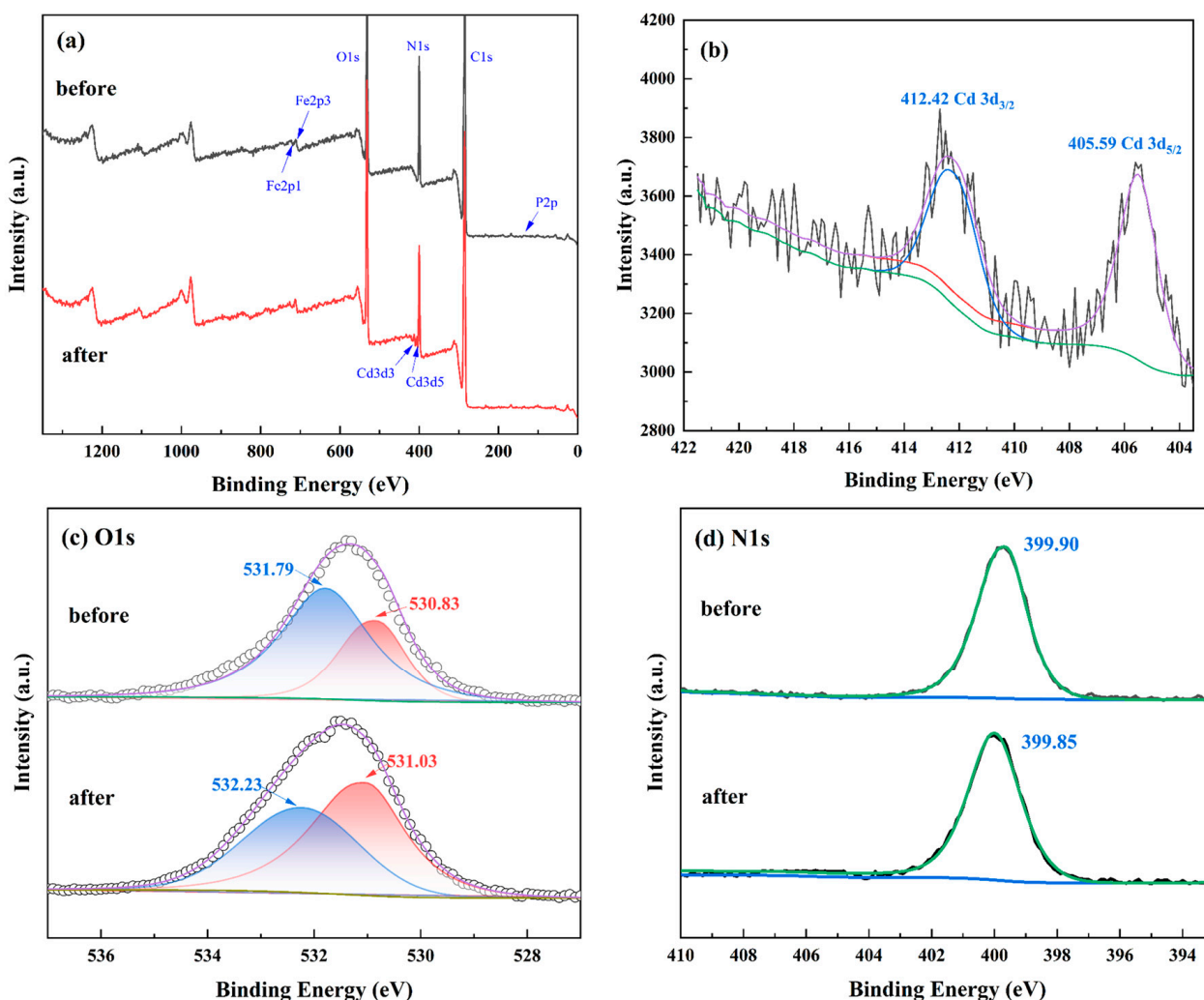


**Figure 19.** XPS spectra for IIP before and after Cd(II) adsorption (a), adsorption and XPS spectra for Cd3d (b), and high-resolution XPS spectra for O1s (c) and N1s (d) for IIP before and after adsorption of Cd(II).

The Fukui function calculated with DFT was used for further verification of the chelating sites of the PBTCA<sup>5-</sup> molecule. Figure 20 shows the geometry optimization of PBTCA<sup>5-</sup> and the Fukui functions ( $f^-$ ) of atoms on potential adsorption sites in PBTCA<sup>5-</sup>.

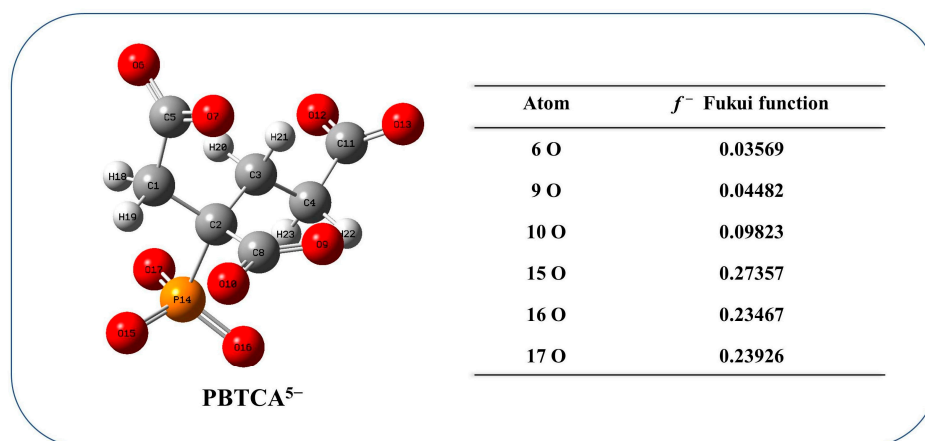


**Figure 20.** DFT calculations: geometric optimization of PBTCA and Fukui function ( $f^-$ ).

The results indicated that one O atom of the C-O group in the carboxyl group and two O atoms of the P-O groups in the phosphonate group in the PBTCA<sup>5-</sup> molecule had high  $f^-$  values, and their electrons were more easily attacked by Cd(II), which constructed the specific binding sites and captured Cd(II) ions by chelation [47]. It should be noted that, although the third O atom in the phosphonate group also had a high  $f^-$  value, it could not be coordinated with Cd(II) due to the steric effect. This result was consistent with the results of the XPS analysis.

The changes in bond lengths and Wiberg bond orders before and after adsorption also reflected the mechanism of Cd(II) adsorption on the imprinted polymer, and the results are listed in Table 7. The results showed that the bond lengths of the C-O bonds in the carboxyl group and the P-O bonds in the phosphonate group increased and the Wiberg bond orders were weakened after the adsorption of Cd(II). These changes were caused by the electron transfer from the O atoms of the carboxyl group and the phosphonate group to the vacant orbitals of Cd(II) following Cd(II) adsorption.

**Table 7.** Partial bond lengths and Wiberg bond orders for PBTCA<sup>5-</sup> and PBTCA-Cd(II).

Items	Bond Length (Å)			Wiberg Bond Order		
	C8-O10	P14-O16	P14-O17	C8-O10	P14-O16	P14-O17
PBTCA <sup>5-</sup>	1.262	1.530	1.532	2.394	2.136	2.112
PBTCA-Cd(II) <sup>3-</sup>	1.287	1.577	1.579	2.193	2.126	1.827

### 3.8. Comparison with Other Adsorbents for Cadmium Adsorption

The adsorption performance of Fe<sub>3</sub>O<sub>4</sub>@SiO<sub>2</sub>@IIP contrasted with that of other sorbents reported in the literature. As seen from Table 8, the Cd(II) adsorption ability of the Fe<sub>3</sub>O<sub>4</sub>@SiO<sub>2</sub>@IIP was superior or equivalent to other adsorbents with regard to equilibrium time and absorption capacity. Furthermore, the imprinted polymer prepared in this study could be easily recovered owing to the efficient and quick magnetic separation. Moreover, the ecofriendly and easy manufacturing methods, as well as the high chemical and thermal stability, will provide Fe<sub>3</sub>O<sub>4</sub>@SiO<sub>2</sub>@IIP with a wide range of applications in a variety of scientific fields.

**Table 8.** Comparison of maximum adsorption capacities of Fe<sub>3</sub>O<sub>4</sub>@SiO<sub>2</sub>@IIP for Cd(II) with other adsorbents reported in the literature.

Adsorbent	Adsorption Capacity (mg·g <sup>-1</sup> )	Equilibrium Time (min)	Ref
Ion-imprinted polydopamine-coated magnetic graphene oxide	17.5	15	[48]
IIHP-VIN-MP	16.99	-	[49]
Vermiculite-600	8.50	120	[50]
MgO-ATP	24.50	180	[51]
Serpentine-700	17.68	120	[52]
C-ATP-SO <sub>4</sub> <sup>2-</sup>	13.29	120	[53]
C-ATP-Cl <sup>-</sup>	17.83	120	[53]
Fe <sub>3</sub> O <sub>4</sub> @SiO <sub>2</sub> @IIP	29.82	20	This work

#### 4. Conclusions

A novel magnetic core-shell Cd(II) surface-imprinted polymer was synthesized using Cd(II) as a template, Fe<sub>3</sub>O<sub>4</sub> as a matrix, MBA as a crosslinker, and PBTCA as a functional monomer by employing the surface imprinting technique and chemical grafting. The imprinted polymer was used to remove Cd(II) from aqueous solution, and the following conclusions were drawn. The introduction of carboxyl and phosphonic acid groups to the surface of Fe<sub>3</sub>O<sub>4</sub>@SiO<sub>2</sub>@IIP was confirmed. The pH value of the system played a crucial role in Cd(II) adsorption. The adsorption capacity increased with increases in pH value, with the maximum adsorption capacity reached at pH = 6.0. The kinetic adsorption process was described with pseudo-second kinetics as it was considered a chemisorption process. The Langmuir model fit the adsorption isotherm data best, implying a monolayer adsorption process. Thermodynamic studies demonstrated that the adsorption process was spontaneous, with an increase in entropy. Although PBTCA had low affinity for Cd(II), the imprinted polymer exhibited superior selectivity for Cd(II) compared to the non-imprinted polymer owing to the specificity obtained from the imprinting technique and dominated over the selective adsorption of Cd(II) from other interfering metal ions. Results from XPS and DFT calculations indicated that O atoms in the carboxyl and phosphonic acid groups in PBTCA were involved in the Cd(II) adsorption. Hence, Fe<sub>3</sub>O<sub>4</sub>@SiO<sub>2</sub>@IIP was proved to be a potential adsorbent for the rapid and selective adsorption and recovery of Cd(II) from aqueous solutions.

**Author Contributions:** Conceptualization, H.H.; methodology, X.D., W.L., and H.H.; software, S.Y. and W.Z.; validation, S.Y., W.Z., and W.L.; formal analysis, H.H., Y.L., and S.Y.; investigation, W.Z. and Y.Z.; resources, X.H. and G.H.; data curation, S.Y. and W.Z.; writing—original draft preparation, S.Y.; writing—review and editing, H.H.; visualization, S.Y. and W.Z.; supervision, Y.Z.; project administration, H.H.; funding acquisition, H.H. and X.D. All authors have read and agreed to the published version of the manuscript.

**Funding:** This research was funded by the Applied Basic Research Project of Yunnan (no. 202001BA070001-120), the Scientific Research Project of Kunming University (no. YJL20025), the Scientific Research Fund of Education Department of Yunnan Province (no. 2023Y0898, 2022Y756, and 2022Y761), the Projects of Yunnan Key Laboratory of Metal-Organic Molecular Materials and Device (no. YN-MOMD2206 and YNMOMD2210), the Open Project of Yunnan Precious Metals Laboratory Co., Ltd. (no. YPML-2023050243), and the Joint Basic Research Program (partial) of Yunnan Provincial Undergraduate Universities (no. 202101BA070001-052).

**Institutional Review Board Statement:** Not applicable.

**Data Availability Statement:** The data presented in this study are available on request from the corresponding author.

**Conflicts of Interest:** The authors declare no conflict of interest.

## References

1. Olympio, K.P.K.; Silva, J.P.d.R.; da Silva, A.S.; Souza, V.C.d.O.; Buzalaf, M.A.R.; Barbosa, F., Jr.; Cardoso, M.R.A. Blood Lead and Cadmium Levels in Preschool Children and Associated Risk Factors in São Paulo, Brazil. *Environ. Pollut.* **2018**, *240*, 831–838. [[CrossRef](#)] [[PubMed](#)]
2. Perera, P.C.T.; Sundarabharathy, T.V.; Sivananthawerl, T.; Kodithuwakku, S.P.; Edirisinghe, U. Arsenic and Cadmium Contamination in Water, Sediments and Fish Is a Consequence of Paddy Cultivation: Evidence of River Pollution in Sri Lanka. *Achiev. Life Sci.* **2016**, *10*, 144–160. [[CrossRef](#)]
3. Shen, X.; Chen, X. Membrane-Free Electrodeionization Using Phosphonic Acid Resin for Nickel Containing Wastewater Purification. *Sep. Purif. Technol.* **2019**, *223*, 88–95. [[CrossRef](#)]
4. Islam, M.A.; Awual, M.R.; Angove, M.J. A Review on Nickel(II) Adsorption in Single and Binary Component Systems and Future Path. *J. Environ. Chem. Eng.* **2019**, *7*, 103305. [[CrossRef](#)]
5. Cao, H.; Yang, P.; Ye, T.; Yuan, M.; Yu, J.; Wu, X.; Yin, F.; Li, Y.; Xu, F. Recognizing Adsorption of Cd(II) by a Novel Core-Shell Mesoporous Ion-Imprinted Polymer: Characterization, Binding Mechanism and Practical Application. *Chemosphere* **2021**, *278*, 130369. [[CrossRef](#)]
6. Zhu, F.; Li, L.; Xing, J. Selective Adsorption Behavior of Cd(II) Ion Imprinted Polymers Synthesized by Microwave-Assisted Inverse Emulsion Polymerization: Adsorption Performance and Mechanism. *J. Hazard. Mater.* **2017**, *321*, 103–110. [[CrossRef](#)] [[PubMed](#)]
7. Zhu, S.; Xi, C.; Zhang, Y.; Zhang, F. Preparation and Characterization of Cadmium(II) -Ion-Imprinted Composites Based on Epoxy Resin. *ACS Appl. Polym. Mater.* **2022**, *4*, 9284–9293. [[CrossRef](#)]
8. Jakavula, S.; Biata, N.R.; Dimpe, K.M.; Pakade, V.E.; Nomngongo, P.N. A Critical Review on the Synthesis and Application of Ion-Imprinted Polymers for Selective Preconcentration, Speciation, Removal and Determination of Trace and Essential Metals from Different Matrices. *Crit. Rev. Anal. Chem.* **2022**, *52*, 314–326. [[CrossRef](#)]
9. Zhu, C.; Hu, T.; Tang, L.; Zeng, G.; Deng, Y.; Lu, Y.; Fang, S.; Wang, J.; Liu, Y.; Yu, J. Highly Efficient Extraction of Lead Ions from Smelting Wastewater, Slag and Contaminated Soil by Two-Dimensional Montmorillonite-Based Surface Ion Imprinted Polymer Absorbent. *Chemosphere* **2018**, *209*, 246–257. [[CrossRef](#)]
10. Ding, C.; Deng, Y.; Merchant, A.; Su, J.; Zeng, G.; Long, X.; Zhong, M.-E.; Yang, L.; Gong, D.; Bai, L.; et al. Insights into Surface Ion-Imprinted Materials for Heavy Metal Ion Treatment: Challenges and Opportunities. *Sep. Purif. Rev.* **2023**, *52*, 123–134. [[CrossRef](#)]
11. Liu, Y.; Meng, X.; Luo, M.; Meng, M.; Ni, L.; Qiu, J.; Hu, Z.; Liu, F.; Zhong, G.; Liu, Z.; et al. Synthesis of Hydrophilic Surface Ion-Imprinted Polymer Based on Graphene Oxide for Removal of Strontium from Aqueous Solution. *J. Mater. Chem. A* **2015**, *3*, 1287–1297. [[CrossRef](#)]
12. Msaadi, R.; Ammar, S.; Chehimi, M.M.; Yagci, Y. Diazonium-Based Ion-Imprinted Polymer/Clay Nanocomposite for the Selective Extraction of Lead (II) Ions in Aqueous Media. *Eur. Polym. J.* **2017**, *89*, 367–380. [[CrossRef](#)]
13. Mishra, S.; Verma, N. Surface Ion Imprinting-Mediated Carbon Nanofiber-Grafted Highly Porous Polymeric Beads: Synthesis and Application towards Selective Removal of Aqueous Pb(II). *Chem. Eng. J.* **2017**, *313*, 1142–1151. [[CrossRef](#)]
14. Sebastian, M.; Mathew, B. Ion Imprinting Approach for the Fabrication of an Electrochemical Sensor and Sorbent for Lead Ions in Real Samples Using Modified Multiwalled Carbon Nanotubes. *J. Mater. Sci.* **2018**, *53*, 3557–3572. [[CrossRef](#)]
15. Ebrahimzadeh, H.; Asgharinezhad, A.A.; Moazzen, E.; Amini, M.M.; Sadeghi, O. A Magnetic Ion-Imprinted Polymer for Lead(II) Determination: A Study on the Adsorption of Lead(II) by Beverages. *J. Food Compos. Anal.* **2015**, *41*, 74–80. [[CrossRef](#)]
16. Büyüktiryaki, S.; Keçili, R.; Hussain, C.M. Functionalized Nanomaterials in Dispersive Solid Phase Extraction: Advances & Prospects. *TrAC Trends Anal. Chem.* **2020**, *127*, 115893. [[CrossRef](#)]
17. Xu, Z.-B.; Wang, W.-L.; Huang, N.; Wu, Q.-Y.; Lee, M.-Y.; Hu, H.-Y. 2-Phosphonobutane-1,2,4-Tricarboxylic Acid (PBTCA) Degradation by Ozonation: Kinetics, Phosphorus Transformation, Anti-Precipitation Property Changes and Phosphorus Removal. *Water Res.* **2019**, *148*, 334–343. [[CrossRef](#)] [[PubMed](#)]
18. Cao, Y.; Zhang, S.; Wang, G.; Li, T.; Xu, X.; Deng, O.; Zhang, Y.; Pu, Y. Enhancing the Soil Heavy Metals Removal Efficiency by Adding HPMA and PBTCA along with Plant Washing Agents. *J. Hazard. Mater.* **2017**, *339*, 33–42. [[CrossRef](#)]
19. Huang, Y.; Zheng, H.; Li, H.; Zhao, C.; Zhao, R.; Li, S. Highly Selective Uranium Adsorption on 2-Phosphonobutane-1,2,4-Tricarboxylic Acid-Decorated Chitosan-Coated Magnetic Silica Nanoparticles. *Chem. Eng. J.* **2020**, *388*, 124349. [[CrossRef](#)]
20. Fan, J.-P.; Yu, J.-X.; Yang, X.-M.; Zhang, X.-H.; Yuan, T.-T.; Peng, H.-L. Preparation, Characterization, and Application of Multiple Stimuli-Responsive Rattle-Type Magnetic Hollow Molecular Imprinted Poly (Ionic Liquids) Nanospheres (Fe<sub>3</sub>O<sub>4</sub>@void@PILMIP) for Specific Recognition of Protein. *Chem. Eng. J.* **2018**, *337*, 722–732. [[CrossRef](#)]
21. Chen, Y.; Ma, X.; Peng, J. Highly Selective Removal and Recovery of Ni(II) from Aqueous Solution Using Magnetic Ion-Imprinted Chitosan Nanoparticles. *Carbohydr. Polym.* **2021**, *271*, 118435. [[CrossRef](#)] [[PubMed](#)]
22. Hou, L.; Yang, C.; Rao, X.; Hu, L.; Bao, Y.; Gao, Y.; Zhu, X. Fabrication of Recoverable Magnetic Surface Ion-Imprinted Polymer Based on Graphene Oxide for Fast and Selective Removal of Lead Ions from Aqueous Solution. *Colloids Surf. Physicochem. Eng. Asp.* **2021**, *625*, 126949. [[CrossRef](#)]
23. Zhao, H.; Liang, Q.; Yang, Y.; Liu, W.; Liu, X. Magnetic Graphene Oxide Surface Lithium Ion-Imprinted Material towards Lithium Extraction from Salt Lake. *Sep. Purif. Technol.* **2021**, *265*, 118513. [[CrossRef](#)]

24. Kutluay, S.; Horoz, S.; Şahin, Ö.; Ekinçi, A.; Ece, M.Ş. Highly Improved Solar Cell Efficiency of Mn-doped Amine Groups-functionalized Magnetic Fe<sub>3</sub>O<sub>4</sub>@SiO<sub>2</sub> Nanomaterial. *Int. J. Energy Res.* **2021**, *45*, 20176–20185. [[CrossRef](#)]
25. Nikmah, A.; Taufiq, A.; Hidayat, A.; Sunaryono; Susanto, H. Excellent Antimicrobial Activity of Fe<sub>3</sub>O<sub>4</sub>/SiO<sub>2</sub>/Ag Nanocomposites. *Nano* **2021**, *16*, 2150049. [[CrossRef](#)]
26. He, H.; Gan, Q.; Feng, C. Synthesis and Characterization of a Surface Imprinting Silica Gel Polymer Functionalized with Phosphonic Acid Groups for Selective Adsorption of Fe(III) from Aqueous Solution: ARTICLE. *J. Appl. Polym. Sci.* **2017**, *134*, 45165. [[CrossRef](#)]
27. Cheng, Y.; Nie, J.; Li, J.; Liu, H.; Yan, Z.; Kuang, L. Synthesis and Characterization of Core–Shell Magnetic Molecularly Imprinted Polymers for Selective Recognition and Determination of Quercetin in Apple Samples. *Food Chem.* **2019**, *287*, 100–106. [[CrossRef](#)]
28. Khalid, A.; Ahmed, R.M.; Taha, M.; Soliman, T.S. Fe<sub>3</sub>O<sub>4</sub> Nanoparticles and Fe<sub>3</sub>O<sub>4</sub>@SiO<sub>2</sub> Core-Shell: Synthesize, Structural, Morphological, Linear, and Nonlinear Optical Properties. *J. Alloys Compd.* **2023**, *947*, 169639. [[CrossRef](#)]
29. Hussain, M.; Rehan, T.; Goh, K.W.; Shah, S.I.; Khan, A.; Ming, L.C.; Shah, N. Fabrication of a Double Core–Shell Particle-Based Magnetic Nanocomposite for Effective Adsorption-Controlled Release of Drugs. *Polymers* **2022**, *14*, 2681. [[CrossRef](#)] [[PubMed](#)]
30. Fang, Y.; Yuan, X.; Wu, L.; Peng, Z.; Feng, W.; Liu, N.; Xu, D.; Li, S.; Sengupta, A.; Mohapatra, P.K.; et al. Ditopic CMPO-Pillar[5]Arenes as Unique Receptors for Efficient Separation of Americium(III) and Europium(III). *Chem. Commun.* **2015**, *51*, 4263–4266. [[CrossRef](#)] [[PubMed](#)]
31. Sun, N.; Lei, R.; Xu, J.; Kundu, S.C.; Cai, Y.; Yao, J.; Ni, Q. Fabricated Porous Silk Fibroin Particles for PH-Responsive Drug Delivery and Targeting of Tumor Cells. *J. Mater. Sci.* **2019**, *54*, 3319–3330. [[CrossRef](#)]
32. Eskandari, E.; Kosari, M.; Davood Abadi Farahani, M.H.; Khiavi, N.D.; Saeedikhani, M.; Katal, R.; Zarinejad, M. A Review on Polyaniline-Based Materials Applications in Heavy Metals Removal and Catalytic Processes. *Sep. Purif. Technol.* **2020**, *231*, 115901. [[CrossRef](#)]
33. Wang, P.; Cheng, H.; Ding, J.; Ma, J.; Jiang, J.; Huang, Z.; Li, J.; Pang, S.; Guan, C.; Gao, Y. Cadmium Removal with Thio-sulfate/Permanganate (TS/Mn(VII)) System: MnO<sub>2</sub> Adsorption and/or CdS Formation. *Chem. Eng. J.* **2020**, *380*, 122585. [[CrossRef](#)]
34. Li, M.; Zhao, C.; Feng, Q.-Z.; Feng, J.; Meng, X.-J. Experimental and DFT Studies on the Adsorption of Cd(II) Ions from Aqueous Solutions by Nanofiber Modified Thiourea Groups. *Chem. J. Chin. U.* **2021**, *42*, 3680–3691. [[CrossRef](#)]
35. Hu, H.; Ren, Z.; Xi, Y.; Fang, L.; Fang, D.; Yang, L.; Shao, P.; Shi, H.; Yu, K.; Luo, X. Insights into the Role of Cross-Linking Agents on Polymer Template Effect: A Case Study of Anionic Imprinted Polymers. *Chem. Eng. J.* **2021**, *420*, 129611. [[CrossRef](#)]
36. He, H.; Gan, Q.; Feng, C. Preparation and Application of Ni(II) Ion-Imprinted Silica Gel Polymer for Selective Separation of Ni(II) from Aqueous Solution. *RSC Adv.* **2017**, *7*, 15102–15111. [[CrossRef](#)]
37. Ni, C.; Liu, Q.; Ren, Z.; Hu, H.; Sun, B.; Liu, C.; Shao, P.; Yang, L.; Pavlostathis, S.G.; Luo, X. Selective Removal and Recovery of La(III) Using a Phosphonic-Based Ion Imprinted Polymer: Adsorption Performance, Regeneration, and Mechanism. *J. Environ. Chem. Eng.* **2021**, *9*, 106701. [[CrossRef](#)]
38. Ren, Z.; Zhu, X.; Du, J.; Kong, D.; Wang, N.; Wang, Z.; Wang, Q.; Liu, W.; Li, Q.; Zhou, Z. Facile and Green Preparation of Novel Adsorption Materials by Combining Sol-Gel with Ion Imprinting Technology for Selective Removal of Cu(II) Ions from Aqueous Solution. *Appl. Surf. Sci.* **2018**, *435*, 574–584. [[CrossRef](#)]
39. Lee, H.M.; Lee, S.G.; Park, H.R.; Chough, S.H. Sorption Behaviors and Relation between Selectivity and Possible Cavity Shapes of the Molecularly Imprinted Materials. *Microporous Mesoporous Mater.* **2017**, *251*, 42–50. [[CrossRef](#)]
40. Huang, Y.; Gao, M.; Deng, Y.; Khan, Z.H.; Liu, X.; Song, Z.; Qiu, W. Efficient Oxidation and Adsorption of As(III) and As(V) in Water Using a Fenton-like Reagent, (Ferrihydrite) -Loaded Biochar. *Sci. Total Environ.* **2020**, *715*, 136957. [[CrossRef](#)]
41. He, H.-X.; Gan, Q.; Feng, C.-G. An Ion-Imprinted Silica Gel Polymer Prepared by Surface Imprinting Technique Combined with Aqueous Solution Polymerization for Selective Adsorption of Ni(II) from Aqueous Solution. *Chin. J. Polym. Sci.* **2018**, *36*, 462–471. [[CrossRef](#)]
42. Khan, M.I.; Nadeem, I.; Majid, A.; Shakil, M. Adsorption Mechanism of Palbociclib Anticancer Drug on Two Different Functionalized Nanotubes as a Drug Delivery Vehicle: A First Principle’s Study. *Appl. Surf. Sci.* **2021**, *546*, 149129. [[CrossRef](#)]
43. He, X.; Deng, F.; Shen, T.; Yang, L.; Chen, D.; Luo, J.; Luo, X.; Min, X.; Wang, F. Exceptional Adsorption of Arsenic by Zirconium Metal-Organic Frameworks: Engineering Exploration and Mechanism Insight. *J. Colloid Interface Sci.* **2019**, *539*, 223–234. [[CrossRef](#)] [[PubMed](#)]
44. Huo, J.-B.; Yu, G.; Xu, L.; Fu, M.-L. Porous Walnut-like La<sub>2</sub>O<sub>2</sub>CO<sub>3</sub> Derived from Metal-Organic Frameworks for Arsenate Removal: A Study of Kinetics, Isotherms, and Mechanism. *Chemosphere* **2021**, *271*, 129528. [[CrossRef](#)] [[PubMed](#)]
45. Alam, M.S.; Gorman-Lewis, D.; Chen, N.; Flynn, S.L.; Ok, Y.S.; Konhauser, K.O.; Alessi, D.S. Thermodynamic Analysis of Nickel(II) and Zinc(II) Adsorption to Biochar. *Environ. Sci. Technol.* **2018**, *52*, 6246–6255. [[CrossRef](#)]
46. Wu, F.; Pu, N.; Ye, G.; Sun, T.; Wang, Z.; Song, Y.; Wang, W.; Huo, X.; Lu, Y.; Chen, J. Performance and Mechanism of Uranium Adsorption from Seawater to Poly(Dopamine) -Inspired Sorbents. *Environ. Sci. Technol.* **2017**, *51*, 4606–4614. [[CrossRef](#)]
47. Zhang, W.-Y.; Ye, S.-Q.; Yang, X.-T.; Zhu, B.-S.; Li, W.-L.; He, H.-X.; Deng, X.-J. A Recoverable Magnetic Surface Ion-Imprinted Polymer Based on Graphene Oxide for Fast and Selective Adsorption of Ni(II) from Aqueous Solution: Experimental and DFT Calculations. *New J. Chem.* **2023**, *47*, 1197–1208. [[CrossRef](#)]

48. Abdolmohammad-Zadeh, H.; Rahimpour, E.; Pasandideh, Y. Utilizing a Nanocomposite Based on Ion-Imprinted Polydopamine-Coated Magnetic Graphene Oxide for Extraction of Cd(II) and Ni(II) from Water Samples. *J. Anal. Chem.* **2020**, *75*, 967–974. [[CrossRef](#)]
49. Aduino, A.; Khan, S.; Augusto da Silva, M.; Gomes Neto, J.A.; Picasso, G.; Sotomayor, M.d.P.T. Synthesis, Characterization and Application of a Novel Ion Hybrid Imprinted Polymer to Adsorb Cd(II) in Different Samples. *Environ. Res.* **2020**, *187*, 109669. [[CrossRef](#)]
50. Padilla-Ortega, E.; Medellín-Castillo, N.; Robledo-Cabrera, A. Comparative Study of the Effect of Structural Arrangement of Clays in the Thermal Activation: Evaluation of Their Adsorption Capacity to Remove Cd(II). *J. Environ. Chem. Eng.* **2020**, *8*, 103850. [[CrossRef](#)]
51. Huang, R.; Lin, Q.; Zhong, Q.; Zhang, X.; Wen, X.; Luo, H. Removal of Cd(II) and Pb(II) from Aqueous Solution by Modified Attapulgite Clay. *Arab. J. Chem.* **2020**, *13*, 4994–5008. [[CrossRef](#)]
52. Cao, C.-Y.; Liang, C.-H.; Yin, Y.; Du, L.-Y. Thermal Activation of Serpentine for Adsorption of Cadmium. *J. Hazard. Mater.* **2017**, *329*, 222–229. [[CrossRef](#)] [[PubMed](#)]
53. Zhang, Q.; Chu, R.; Wei, Y.; Cai, L. A Comparative Study of Cd(II) Adsorption on Calcined Raw Attapulgite and Calcined Aluminium Hydroxide-Modified Attapulites in Aqueous Solution. *RSC Adv.* **2022**, *12*, 13695–13705. [[CrossRef](#)] [[PubMed](#)]

**Disclaimer/Publisher's Note:** The statements, opinions and data contained in all publications are solely those of the individual author(s) and contributor(s) and not of MDPI and/or the editor(s). MDPI and/or the editor(s) disclaim responsibility for any injury to people or property resulting from any ideas, methods, instructions or products referred to in the content.